

Sustained delivery of 4-phenylbutyric acid via chitosan nanoparticles in foam for decontamination and treatment of lewisite-mediated skin injury

Meheli Ghosh ^a, Nethra Viswaroopan ^a, Sharvari M. Kshirsagar ^a , Jasim Khan ^b, Suha Mohiuddin ^b, Ritesh K. Srivastava ^b , Mohammad Athar ^b, Ajay K. Banga ^{a,*}

^a Center for Drug Delivery Research, Department of Pharmaceutical Sciences, College of Pharmacy, Mercer University, Atlanta, GA 30341, USA

^b UAB Research Center of Excellence in Arsenicals, Department of Dermatology, University of Alabama at Birmingham, Birmingham, AL, USA

ARTICLE INFO

Keywords:
4-Phenylbutyric acid
Lewisite
Foam formulation
Chitosan nanoparticles
Skin delivery
Decontamination

ABSTRACT

Lewisite, a chemical warfare agent, induces severe skin injury by oxidative stress and endoplasmic reticulum (ER) dysfunction, necessitating innovative antidote strategies. This study developed chitosan nanoparticle-loaded foam formulations for rapid skin decontamination and sustained topical delivery of 4-phenylbutyric acid (4-PBA), an ER stress-reducing chaperone. Nanoparticles were synthesized via ionic gelation using low (LMW) and medium molecular weight (MMW) chitosan. The optimized formulations, N31 (LMW) and N35 (MMW), achieved drug loadings of 5.04 % and 10.09 % w/w, particle sizes of 141.88 ± 26.31 nm and 176.10 ± 36.97 nm, monodisperse distributions ($PDI < 0.3$), high entrapment efficiency (>93 %) and good stability with zeta potential of -16.67 mV and -19.37 mV, respectively. Incorporation into foam enabled both effective decontamination (>70 % efficiency) and sustained 4-PBA delivery. In vitro release studies demonstrated sustained drug release over 24 h. Permeation studies using dermatomed human skin revealed that nanoparticle formulations significantly reduced 4-PBA delivery: N35 decreased permeation by 38.4 % (214.35 ± 16.6 $\mu\text{g}/\text{cm}^2$ vs. 348.10 ± 5.37 $\mu\text{g}/\text{cm}^2$ for free 4-PBA), while N31 reduced it by 81.35 % (64.90 ± 6.89 $\mu\text{g}/\text{cm}^2$). Both formulations retained efficacy in PAO challenged skin, with N35 delivering 158.54 ± 53.93 $\mu\text{g}/\text{cm}^2$ and N31 138.25 ± 14.72 $\mu\text{g}/\text{cm}^2$ over 24 h.

Furthermore, in vivo studies showed that the optimized formulation with N35 chitosan (4-PBA N35 + N-acetyl cysteine (NAC)) significantly protects against PAO-induced skin injury and inflammatory cytokine production in Ptg1 $^{+/-}$ /SKH-1 hairless mice. Thus, the translational feasibility and effective treatment by the foam formulated 4-PBA N35 + NAC against arsenical-induced skin injury is demonstrated.

1. Introduction

Vesicants are chemicals known to cause severe blistering and inflammation of the skin upon contact. Arsenicals are a notable class within this group that were developed as chemical weapons. Due to their relatively easy synthesis and their ability to cause immediate, painful tissue damage, arsenicals are considered as threat agents under the current situation of multiple global conflicts. Some arsenicals produced in the era of world war I/II include lewisite, methylidichloroarsine, phenyldichloroarsine, and ethyldichloroarsine (Srivastava et al., 2016). Lewisite, or 2-chlorovinylidichloroarsine, was particularly favored for its high toxicity and became an important choice for munitions. Despite the cessation of chemical warfare agent development by many countries, lewisite stockpiles still exist globally, posing a risk of accidental or

intentional exposure, which remains a significant public health threat (Karalliedde et al., 2000). Exposure to lewisite can result in immediate skin irritation and redness, progressing to severe pain, inflammation, and blistering within hours (Li et al., 2016). According to the National Defense Research Committee (NDRC), human exposure to liquid lewisite at doses ranging from 3 to 14 μg can cause erythema, while doses of 22–40 μg can lead to blistering, and as little as 2 mL (equivalent to 37.6 mg/kg) applied to adult human skin can be fatal within several hours (Acute Exposure Guideline Levels for Selected Airborne Chemicals, 2016). The most severe injuries typically manifest 36–48 h after exposure, with full recovery taking two to three weeks. Prompt decontamination with running water for up to 10 min is essential for minimizing skin damage but is often difficult for first responders in contaminated areas (Meenu et al., 2020).

* Corresponding author at: 3001 Mercer University Drive, Atlanta, GA 30341, United States.

E-mail address: banga_ak@mercer.edu (A.K. Banga).

The absence of an effective antidote complicates the long-term healing process for lewisite-induced skin injuries. The current antidote, British Anti-Lewisite (BAL) or dimercaprol, is not effective for skin injuries because it needs to be administered systemically as painful intra-muscular injections due to its poor water solubility and inherent toxicity. BAL is also linked with significant side effects such as headaches, nasal congestion, vomiting, chest pain, anxiety, and sweating. Additionally, it has a narrow therapeutic window that is both dose- and time-dependent. Although water-soluble derivatives of BAL have been developed to reduce toxicity, they have shown decreased effectiveness against lewisite-induced skin damage (Peters et al., 1945; Peters, 1948). Therefore, there is a critical need to develop a new antidote formulation that can effectively decontaminate lewisite and deliver therapeutic agents directly to the affected skin areas. Such advancements could greatly enhance the ability of first responders to treat injuries caused by lewisite exposure.

Lewisite injury induces endoplasmic reticulum (ER) stress and reactive oxygen species (ROS), triggering the unfolded protein response (UPR) pathway (Srivastava et al., 2016). Sustained UPR activation can result in inflammation, tissue damage, and eventual cell death. 4-phenylbutyric acid (4-PBA), a chemical chaperone approved by the FDA for urea cycle disorders, and N-acetyl-L-cysteine (NAC), an antioxidant has emerged as a promising remedy against lewisite-induced toxicity. By inhibiting the UPR signaling pathway, enhancing protein folding, and alleviating ER stress, 4-PBA helps reduce inflammation and tissue damage. Studies have demonstrated that 4-PBA treatment effectively reduces inflammation and blistering caused by skin exposure to phenylarsine oxide (PAO), a lewisite surrogate (Stone et al., 2016; Dandekar et al., 2023). While 4-PBA is currently available in oral tablet form, this route of administration presents several challenges, including low bioavailability, poor patient compliance, potential systemic side effects, and swallowing difficulties (Ghosh and Banga, 2025). Moreover, topical formulations are essential for decontaminating lewisite-exposed skin (Stone et al., 2016). Given these limitations, developing alternative 4-PBA formulations for skin application is crucial. Such formulations could provide both localized actions at the application site and systemic effects following absorption, which can also be tailored to allow immediate lewisite decontamination from the skin (Bhattacharjee et al., 2025). This approach may enhance 4-PBA's therapeutic efficacy while mitigating drawbacks associated with oral administration.

4-PBA is a moderately lipophilic molecule with a molecular weight of 162.204 g/mol, a log P value of 2.5, and a melting point of approximately 50 °C. Its favorable physicochemical properties enable rapid permeation into and across dermatomed porcine and human skin (Kshirsagar et al., 2024). However, while this addresses systemic effects of lewisite, it may not adequately treat skin injuries. Previous research has explored various chemical and physical enhancement techniques for transdermal 4-PBA delivery, including encapsulation in microsponge formulations (Kshirsagar et al., 2024). However, direct skin application of 4-PBA may cause irritation or sensitization. Encapsulating 4-PBA in nanoparticles could potentially eliminate skin irritation issues while offering advantages over microsponges, such as improved skin penetration, increased bioavailability, and enhanced retention time in skin layers (Sintov and Shapiro, 2004; Li et al., 2016; Ghosh et al., 2024). This approach may address both skin injuries and systemic effects caused by lewisite exposure. A previous study developed a blank placebo topical foam formulation (F30) for rapid and effective decontamination of PAO (Vora et al., 2022). However, this formulation contained sodium lauryl ether sulfate, an anionic foaming agent (surfactant), for use as an inactive ingredient in drug products and can show potential skin irritation. Thus, the present study aims to encapsulate 4-PBA in polymeric nanoparticles and evaluate the effects of formulation and process parameters on drug loading, entrapment, zeta potential, polydispersity index, and particle size. Additionally, the study seeks to modify the previously developed foam formulation by replacing the foaming agent with a non-ionic, non-irritant, alternative and incorporate optimized 4-

PBA-loaded nanoparticles to achieve decontamination of the lewisite followed by sustained delivery of 4-PBA into and across the skin (Kumar et al., 2022; Alkholief et al., 2023).

In this study, we investigated the use of chitosan for nanoparticle formation to encapsulate 4-PBA. Chitosan, a natural cationic polysaccharide, possesses several advantageous properties, including biodegradability, non-toxicity, hemostatic and antimicrobial activity, bio-adhesive and penetration-enhancing characteristics. These attributes make chitosan a promising candidate for controlled drug release applications. The unique polymer structure of chitosan allows for the development of nanoparticles capable of sustained drug release over extended periods. As the nanoparticles gradually degrade, they can be safely metabolized and eliminated by the body (Michailidou et al., 2019). Additionally, chitosan's mucoadhesive properties may enhance its retention on the skin, potentially increasing the contact time of the drug formulation with the affected area and extending the duration of drug release (Al-Kassas et al., 2016). Chitosan nanoparticles offer versatility in formulation, allowing for the optimization of drug loading and release profiles. Recent research has shown a growing interest in using chitosan Nanoparticles as carriers for active components in both cosmetics and skin drug delivery. Studies have explored the use of chitosan nanoparticles for treating various skin disorders, including malignant melanoma and infections, as well as systemic conditions such as diabetes and hypertension (Ma et al., 2022; Jafernik et al., 2023). In our study, we compared two molecular weights of chitosan – low molecular weight (LMW) and medium molecular weight (MMW) – in nanoparticle formation, *In-vitro* release, and permeation studies. By encapsulating 4-PBA in chitosan nanoparticles, we aimed to achieve more controlled and prolonged release compared to conventional formulations. This approach can potentially enhance therapeutic efficacy and reduce dosing frequency in treating lewisite-induced injuries, offering a promising strategy for improved patient outcomes.

Chitosan nanoparticles can be prepared using various techniques, such as ionotropic gelation, polyelectrolyte complexing, emulsification, solvent diffusion, and micro emulsification. Among these methods, ionic gelation is one of the most popular methods because it is cost-effective, non-toxic, and does not require organic solvents. Furthermore, it allows for flexible and precise control over particle size and drug loading. The ionic gelation process involves the formation of inter- and intramolecular linkages between chitosan's positively charged primary amino groups and the negatively charged components of cross-linkers, typically sodium tripolyphosphate (TPP) (Abdel-Hafez et al., 2018; Ta et al., 2021). This interaction leads to the spontaneous formation of chitosan nanoparticles. Several factors influence the properties of nanoparticles produced by ionic gelation. These include the stirring speed, ratio of chitosan to cross-linker, and the concentrations of polymer, drug, and cross-linker. By adjusting these variables, one can fine-tune nanoparticle characteristics to meet specific application requirements. Additionally, the molecular weight of chitosan plays a crucial role in determining various parameters in nanoparticle formation, like particle size and drug loading (Hasanovic et al., 2009). Given these advantages, we employed the ionic gelation technique in our study to develop 4-phenylbutyric acid-loaded chitosan nanoparticles.

The effectiveness of the optimized 4-PBA loaded chitosan nanoparticles in foam formulation was evaluated through *In-vitro* and *In-vivo* studies using Franz diffusion cells and a hairless mouse model, respectively. The mice were exposed to PAO, a surrogate for lewisite, and the treatment's efficacy was assessed by examining changes in gross skin injury, epidermal cell apoptosis, and cytokine levels in the skin tissue. This approach aimed to create a potential antidote for skin injuries caused by lewisite or other arsenical chemical warfare agents. The study demonstrated the feasibility of this innovative formulation as a promising decontamination and treatment option for such chemical-induced skin damage.

Table 1
Formulation matrix for 4-PBA loaded chitosan nanoparticles.

Formulation	Chitosan type	Chitosan %	TPP %	Drug: Polymer	TPP injection rate (mL/min)
N1	MMW	1.0	0.08	2:01	2.0
N2	LMW	0.2	0.08	2:01	2.0
N3	MMW	0.2	0.08	2:01	2.0
N4	MMW	0.2	0.02	2:01	2.0
N5	LMW	0.2	0.02	2:01	2.0
N6	MMW	1.0	0.02	2:01	2.0
N7	LMW	1.0	0.02	2:01	2.0
N8	MMW	2.0	0.08	2:01	2.0
N9	MMW	2.0	0.02	2:01	2.0
N10	LMW	1.0	0.08	2:01	2.0
N11	LMW	0.2	0.05	1:02	2.0
N12	MMW	0.2	0.05	1:02	2.0
N13	LMW	0.8	0.20	1:02	2.0
N14	MMW	0.8	0.20	1:02	2.0
N15	LMW	0.2	0.05	1:02	2.0
N16	MMW	0.2	0.05	1:02	2.0
N17	LMW	0.8	0.20	1:02	2.0
N18	MMW	0.8	0.20	1:02	2.0
N19	LMW	2.0	0.08	2:01	1.0
N20	MMW	2.0	0.08	2:01	1.0
N21	LMW	2.0	0.02	2:01	1.0
N22	MMW	2.0	0.02	2:01	1.0
N23	LMW	1.0	0.08	2:01	1.0
N24	MMW	1.0	0.08	2:01	1.0
N25	LMW	1.0	0.02	2:01	1.0
N26	MMW	1.0	0.02	2:01	1.0
N27	LMW	1.0	0.10	2:01	1.0
N28	MMW	1.0	0.10	2:01	1.0
N29	LMW	0.3	0.08	2:01	1.0
N30	LMW	0.3	0.05	2:01	1.0
N31	LMW	0.5	0.08	2:01	1.0
N32	LMW	0.5	0.05	2:01	1.0
N33	MMW	0.3	0.08	2:01	1.0
N34	MMW	0.3	0.05	2:01	1.0
N35	MMW	0.5	0.08	2:01	1.0
N36	MMW	0.5	0.05	2:01	1.0
N37	LMW	0.3	0.08	2:01	1.0
N38	MMW	0.2	0.08	2:01	1.0

2. Materials and methods

2.1. Materials

4-PBA, TPP, LMW chitosan 75–85 % deacetylated, mol wt 50,000–190,000 Da based-on viscosity) and MMW chitosan (75–85 % deacetylated, mol wt 190,000–310,000 Da based-on viscosity) were

$$\% \text{ Encapsulation efficiency (EE)} = \frac{\text{Total amount of 4PBA used} - \text{Free drug amount}}{\text{Total amount of 4PBA used}} * 100$$

purchased from Sigma Aldrich (Saint Louis, MO, USA). Organic solvents such as acetonitrile and ethanol were purchased from Pharmaco-aaper (Brookfield, CT, USA). Dermatomed human skin was procured from a tissue bank under a protocol exempted by the Mercer University Institutional Review Board (H25-03003). Disodium hydrogen phosphate (Na_2HPO_4), Tween 20, and phosphate-buffered saline, pH 7.4 (PBS) were acquired from Fisher Scientific. Propylene glycol (PG) was purchased from EKICHEM (Joliet, IL, USA). Oleic acid (OA) was gifted by Croda Inc. (Edison, NJ, USA).

2.2. Formulation of 4-PBA-loaded chitosan nanoparticles

Chitosan nanoparticle formulations (N1-N38) were synthesized using the ionic gelation method (Al-Kassas et al., 2016), employing both

LMW and MMW chitosan. Key formulation parameters, including drug-polymer ratios (2:1 and 1:2), crosslinker concentrations (0.08 %, 0.02 %, and 0.05 % TPP), polymer type (LMW or MMW), chitosan concentrations (2 %, 1 %, 0.8 %, 0.5 %, 0.3 %, and 0.2 %), and process conditions such as TPP injection rate (2 mL/min and 1 mL/min) and stirring speed, were optimized as detailed in Table 1. The synthesis process involved dissolving chitosan in acetic acid adjusted to pH 4.5, followed by the controlled injection of a 4-PBA solution in ethanol using a syringe pump under magnetic stirring at 1200 rpm. Subsequently, an equal volume of TPP solution was added dropwise to the chitosan solution under stirring at 650 rpm, resulting in the immediate formation of nanoparticles. These nanoparticles were collected after centrifugation at 25,000 rpm for 20 min, washed twice with deionized water to remove excess drug and TPP, and then lyophilized for further analysis.

2.3. Characterization of 4-PBA-loaded chitosan nanoparticles

Extensive characterization of all nanoparticle batches (N1-N38) was conducted to assess drug loading, encapsulation efficiency, particle size, polydispersity index (PDI), and zeta potential. Batches exhibiting optimal characteristics were selected for further analysis using scanning electron microscopy (SEM), Fourier-transform infrared spectroscopy (FTIR), and differential scanning calorimetry (DSC). Additionally, stability studies were performed to evaluate their long-term performance.

2.3.1. Determination of particle size, PDI, and zeta potential

Particle size, PDI, and zeta potential measurements were conducted using a Malvern ZEN3600 ZetaSizer. For particle size and PDI analysis, samples were placed in a four-sided clear cuvette, with measurements taken at a scattering angle of 173°. Each sample was analyzed in three runs, consisting of ten sets of 5-second measurements per run. Zeta potential was determined using a folded capillary cell, with three runs of ten measurements per sample. All samples were analyzed in triplicate, and the average results were calculated to ensure accuracy.

2.3.2. Evaluation of percent encapsulation efficiency

The entrapment efficiency of 4-PBA was determined by quantifying the amount of free drug remaining in the supernatant after centrifugation, as outlined in Section 2.2. The supernatants were diluted and analyzed using a validated HPLC method to measure the recovered 4-PBA. Entrapment efficiency was calculated using the formula provided below.

2.3.3. Evaluation of percent drug loading

The percentage drug loading of 4-PBA in chitosan nanoparticles was determined by dispersing a known weight of lyophilized nanoparticles in ethanol. After centrifugation at 13,500 RPM for 10 min, the mixture was filtered, and the filtrate was analyzed using a validated HPLC method. The % drug loading was calculated using the formula provided below.

$$\% \text{ Drug Loading} = \frac{\text{Amount of the drug in nanoparticle (mg)}}{\text{Weight of the nanoparticle taken (mg)}} * 100$$

2.3.4. SEM studies

SEM analysis was performed at the Emory University Robert P. Apkarian Integrated Electron Microscopy Core Facility in Atlanta, GA,

USA. For analysis, 4-PBA-loaded chitosan nanoparticles were suspended in deionized water and applied to a silicon wafer. After drying, the samples were examined using a JEOL JSM-IT700HR scanning electron microscope at various magnifications to assess the shape and surface morphology of the nanoparticles.

2.3.5. Drug-polymer interaction using FTIR analysis

FTIR was employed to investigate the interactions between 4-PBA, chitosan, and TPP. The analysis was conducted in Attenuated Total Reflectance mode, where pure 4-PBA, chitosan (both LMW and MMW), TPP, and the nanoparticles (N31 and N35) were examined. The percentage transmittance was recorded against the wavenumber to identify changes in major functional groups, which would indicate significant interactions between the polymers and 4-PBA in the 4-PBA-loaded chitosan nanoparticles.

2.3.6. Differential scanning calorimetry (DSC)

DSC was performed using a Shimadzu instrument from Japan. Samples were sealed in aluminum pans and scanned from 25 °C to 300 °C under a nitrogen flow of 20 mL/min, with a heating rate of 5 °C/min. An empty aluminum pan served as the reference. The analysis measured heat flow as a function of temperature, providing insight into the efficiency of 4-PBA encapsulation within the chitosan polymer matrix. Temperature calibration was conducted using indium as the standard.

2.4. Stability studies

The optimized nanoparticle batches underwent short-term stability studies under two distinct environmental conditions. The nanoparticles were stored in sealed glass vials within a desiccator at either 40 °C ± 2°C with 75 % RH ± 5 % RH, simulating accelerated degradation conditions, or at 25 °C ± 2°C with 60 % RH ± 5 % RH, serving as an accelerated condition for refrigerated storage. After a month, the nanoparticles stored under both conditions were evaluated for changes in drug content using HPLC, particle size, PDI, zeta potential, and structural integrity via FTIR and DSC.

2.5. Preparation of foam formulation having dispersed 4-PBA loaded chitosan nanoparticles

Our laboratory has previously developed and optimized a foam formulation that demonstrated efficacy in decontaminating lewisite surrogates from skin layers (Vora et al., 2022). However, the foaming agent SLES was replaced with Tween 20, a more commonly used and equally effective surfactant in forming a stable foam. The composition of our revised foam formulation (F39) is detailed in Table 2. We incorporated lyophilized nanoparticles into the foam such that each milliliter of the foam formulation contains 1.5 mg of 4-PBA.

2.6. In-vitro drug release study (IVRT)

IVRT studies were performed using vertical Franz diffusion cells with a permeation area of 9 mm and a 5 mL receptor chamber. A cellulose-based dialysis membrane with a molecular weight cut-off of 14,000 kDa separated the donor and receptor chambers. Phosphate-buffered

saline (PBS) at pH 7.4 was used as the receptor solution, which was continuously stirred at 600 RPM and maintained at 37 °C for 24 h. Two formulations of foam were tested: one containing 4-PBA-loaded LMW chitosan nanoparticles (N31) and the other containing MMW chitosan nanoparticles (N35). Each formulation contained 1.5 mg of 4-PBA per mL of foam. For comparison, unencapsulated 4-PBA in foam (3 mg/2 mL) served as a control. The objective of the release study was to investigate the release kinetics of 4-PBA from the nanoparticles and to compare any differences in release behavior between the LMW and MMW chitosan formulations. Samples were collected from the receptor chamber at predetermined time points (0, 0.25, 0.5, 1, 2, 3, 4, 6, 8, 22, and 24 h) and analyzed using a validated HPLC method.

2.7. Skin preparation and integrity testing

For dermatomed porcine skin, full-thickness skin from porcine ears was separated using a surgical blade and then dermatomed using a Dermatome 75 mm (Nouvag AG, Goldach, Switzerland). Both human and porcine skin samples were stored at -80 °C until use. Prior to experimentation, the skin was thawed in ziplock bags using 10 mM PBS at 37 °C and cut into appropriate-sized pieces. The thickness of each skin piece was measured using a thickness gauge (MTG-DX2 by Checkline, Cedarhurst, NY), with dermatomed skin typically ranging from 200 to 500 µm in thickness.

To ensure the integrity of the skin barrier for in vitro permeation testing (IVPT), the electrical resistance of skin pieces was assessed using a digital multimeter (Agilent Technologies, CA, USA) connected to silver-silver chloride electrodes and an arbitrary waveform generator (Agilent 33220A, 20 MHz Function). This method, previously developed by our group, involves mounting skin pieces in vertical Franz diffusion cells filled with 10 mM PBS at pH 7.4, with 300 µL in the donor chamber and 5 mL in the receptor chamber. After a 10-minute equilibration period, electrodes were immersed in both chambers, and a load resistor (R_L) was connected in series with the skin sample (Radmard et al., 2024). The voltage changes across the entire circuit (V_O), and the skin (V_S) was measured using the multimeter. Skin resistance was calculated using the formula:

$$R_S = V_S R_L / (V_O - V_S),$$

where R_L and V_O are 100 kΩ and 100 mV, respectively.

Skin pieces with resistance below 10 kΩ cm² were excluded from further studies.

2.8. In-vitro permeation testing (IVPT)

IVPT was conducted using vertical Franz diffusion cells, following a procedure similar to that employed in the drug release studies. Skin pieces were secured between the donor and receptor chambers, and the system was maintained at 37 °C using a circulating water jacket. The skin surface temperature was kept at 32 °C, as verified by an infrared thermometer. An infinite dose (200 µL) of each formulation was applied to the skin using a pipette. The formulations included unencapsulated 4-PBA as a control, 4-PBA nanoparticles suspended in PBS, and 4-PBA nanoparticles suspended in foam formulations, all with a 4-PBA concentration of 1.5 mg/mL. Receptor samples were collected at predetermined intervals over 24 h from the sampling arm. After each collection, the sample volume was replaced with 300 µL of fresh receptor media to maintain sink conditions. The collected samples were analyzed using a validated HPLC method.

2.8.1. IVPT to determine sustained delivery 4-PBA from chitosan nanoparticles

An IVPT study was conducted to compare the permeation of 4-PBA from different foam formulations. The formulations included pure 4-PBA, 4-PBA loaded LMW chitosan nanoparticles (N31), and 4-PBA

Table 2

Composition of the Foam formulation having 4-PBA loaded chitosan nanoparticles.

	Foam (f39)
Tween 20, Foaming Agent (%w/v)	15
Ethanol (%v/v)	10
Oleic acid (%v/v)	5
Propylene glycol (%v/v)	70

loaded MMW chitosan nanoparticles (N35). This study aimed to investigate how encapsulation in chitosan nanoparticles affects the permeation of 4-PBA compared to the free drug in a foam formulation. Additionally, to assess the impact of the vehicle on sustained delivery, all three formulations were also tested using PBS as a vehicle. This approach provided insights into whether the sustained delivery observed is due to the foam formulation itself or the encapsulation within chitosan nanoparticles. Furthermore, the study allowed for a comparison of the permeation differences between LMW and MMW chitosan formulations.

2.8.2. IVPT using different skin types

An IVPT study was conducted to investigate the impact of different skin types on the delivery of 4-PBA from chitosan nanoparticles. 4-PBA loaded nanoparticles (both LMW and MMW) were tested in two types of skin: dermatomed porcine skin and dermatomed human skin. These formulations were applied in both foam and PBS vehicles, with the latter serving as controls. Prior to testing, the thickness and integrity of each skin sample were evaluated to ensure consistency. The study aimed to quantify the amount of 4-PBA delivered across the skin from these formulations, providing insights into how different skin types influence drug permeation.

2.8.3. IVPT to determine decontamination efficiency

A previously established protocol in our laboratory was utilized to assess the decontamination efficacy of various formulations against PAO. The protocol involved using Franz diffusion cells under conditions similar to those used in other IVPT studies (Section 2.8). Initially, 100 µL of PAO dissolved in ethanol (100 mg/mL) was added to the donor chamber using a micropipette, and the compartment was left open to simulate in vivo conditions. Receptor samples (300 µL) were collected at 0 and 30 min after PAO exposure, with an equal volume of fresh receptor solution added after each sampling. Following 30 min of PAO exposure, 100 µL of different foam formulations was applied to the donor chamber for 5 min to facilitate decontamination. The formulation was then removed from the skin surface using cotton buds, and the donor chamber was replaced. The skin was rinsed three times with 1 mL of 10 mM PBS, dried with cotton buds, and then cut, minced, and extracted with 2 mL of methanol on a platform shaker at 150 rpm for four hours. The extracts were filtered using 0.22 µm membrane nylon filters and analyzed by HPLC. A control group, where PAO-exposed skin was not treated with any formulation, served as a reference to calculate the percentage decontamination efficacy.

The decontamination efficiency of the formulations was calculated using the formula:

$$\text{Decontamination Efficiency (\%)} = \frac{\text{Amount (after exposure)} - \text{Amount (after decontamination)}}{\text{Amount (after exposure)}} * 100$$

where "Amount after Exposure" is the total PAO delivered into the skin after 30 min, and "Amount after Decontamination" is the PAO remaining in the skin after treatment with the test formulation.

2.8.4. IVPT to determine permeation of 4-PBA after lewisite (PAO) exposure to skin

An IVPT study was conducted to examine how exposure to PAO affects the delivery of 4-PBA from chitosan nanoparticles through skin. The study involved testing pure 4-PBA and 4-PBA-loaded nanoparticles formulated in foam. The experimental design included exposing the skin to PAO for 30 min, followed by a 5-minute decontamination treatment using foam formulations. After decontamination, the skin was washed to

remove any residual decontamination formulation, and then the same foam formulations were reapplied. The permeation of 4-PBA into and across the skin was monitored over 24 h to assess how PAO exposure impacts 4-PBA delivery from these formulations.

2.9. Quantitative analysis using high-performance liquid chromatography

Quantification of 4-PBA and PAO was conducted using a validated HPLC method developed in our laboratory. The analysis employed a Waters 2695 Separation module equipped with a 996 Photo Diode Array UV detector and an Agilent Eclipse C18 column (150 × 4.6 mm, 5 µm particle size). The mobile phase consisted of acetonitrile and 10 mM disodium hydrogen phosphate at pH 7, in a ratio of 15:85, under isocratic conditions. The column temperature was maintained at 35 °C, with an optimized flow rate of 1.2 mL/min and a constant injection volume of 10 µL. Each injection had a total run time of 10 min. The retention time for 4-PBA and PAO was approximately 5.5 and 3.9 min, respectively.

2.10. Lag time calculation

Lag time refers to the time it takes for a drug to begin permeating from the donor chamber across the skin into the receptor chamber. To calculate the lag time for the permeation of 4-PBA from control and nanoparticle formulations, the linear portion of the cumulative drug permeation versus time plot was extrapolated. By setting the y-variable (cumulative drug permeation) to zero, the corresponding x-variable (time) was determined from the linear equation, thereby calculating the lag time.

2.11. Efficacy evaluation of foam formulated, 4-PBA N35 + NAC against PAO-induced skin injury in mice

In vivo experiments were conducted utilizing an equal number of male and female *Ptch1*+/−-SKH-1 hairless mice (N = 6/group) following the approved protocol of the Institutional Animal Ethics Committee of the University of Alabama at Birmingham. Before starting in vivo experiments, animals were randomized and assigned to their corresponding groups. The animals were divided into 4 groups. Group-1 and 2 received a topical application of either vehicle control (30 µL ethanol) or ethanol-diluted PAO (100 µg/mouse in 30 µL) respectively on a 2 × 2 cm² area of dorsal skin as described earlier (Kshirsagar et al., 2024; Srivastava et al., 2021). While group 2 and 3 received placebo and drug treatment respectively 30-minute following PAO challenge to the skin. Drug formulations were prepared by dispersion of 4-PBA loaded chito-

san nanoparticles in F39 foam formulation which contained an antioxidant, NAC (4-PBA N35 + NAC). In this drug formulation, the amount of 4-PBA loaded in N35 was calculated based on maximum occupancy of 4-PBA in these chitosan nanoparticles (2.31 mg nanoparticle contained 150 µg 4-PBA/100 µL foam) while we used NAC (15 mg/100 µL foam) based on our previous published data (Dandekar et al., 2023). In addition to testing drug containing formulation, the placebo formulation was also identically tested in parallel. Placebo was prepared using chitosan nanoparticle (N35) dispersed in F39 foam formulation but without drug agents, 4-PBA and NAC. To evaluate the efficacy of formulated drug namely, 4-PBA N35 + NAC was applied topically (100 µL) to anaesthetized mouse skin over the area 2 × 2 cm² of PAO exposure. Twenty-four hours after, all the animals of groups 1–4 were clinically assessed

for skin injury and data were reported as changes in Draize scores (combine effects of erythema, edema, and necrosis). Before the termination of experiment, mouse exposed skin was photographed for capturing gross cutaneous injury. At the end of the experiment, mice were euthanized, skin and tissues harvested for analysis of protective effects of 4-PBA N35 + NAC against PAO-induced inflammation and tissue damage. Histological evaluation was performed on H&E-stained tissue sections on a Keyence fluorescence microscope (Model BZ-X710, Osaka, Japan). Apoptosis was assessed using TUNEL assay with a commercial detection kit (Roche Diagnostics, Indianapolis, IN, USA). Cytokine levels measured using MILLIPLEX® Mouse Cytokine/Chemokine kit (MCYTMAg-70K-PX32; EMD Millipore). Assay was performed on a MAGPIX Luminex system according to the manufacturer's protocol. Skin lysates were prepared, protein concentration was measured, and equal amount of protein was used for western blot analysis of various proteins ATF4 (Cat No. 118157, cell signaling) CHOP (Cat No. 2895, cell signaling), p-eIF2 α (Cat No. 3398, cell signaling), Cleaved caspase-3 (NB100-56708, Novus biologicals). GAPDH (Cat No. 2118, cell signaling) was used as endogenous control. Immunohistochemistry analysis of ATF4 (MA5-32364, Thermo Fisher Scientific) in the mouse skin sectioned were performed using previously described methods (Srivastava et al., 2022). Briefly, skin sections were deparaffinized, rehydrated, and treated with antigen-unmasking solution according to the manufacturer's protocol (Vector Laboratories, Burlingame, CA, USA). Following, washing with PBS, blocking with 1 % BSA with 4 % goat serum, skin sections were incubated with primary antibodies, followed by secondary antibodies and slides were visualized under Keyence microscope using a universal peroxidase-coupled secondary antibody and DAB substrate.

2.12. Statistical analysis

Statistical analysis of the results was conducted using GraphPad Prism software (version 9.4.1, GraphPad Software, San Diego, CA). Data are presented as mean values with standard error (SE), based on sample sizes of $n = 3$ or 4. For comparisons involving multiple groups, one-way analysis of variance (ANOVA) was employed. Subsequent post hoc analyses utilized Tukey's test to compare differences between multiple groups. A p-value of less than 0.05 was considered statistically significant, indicating a significant difference between the test groups.

3. Results

3.1. Formation and characterization of 4-PBA-loaded chitosan nanoparticles

The formed 4-PBA-loaded chitosan nanoparticle batches were characterized for drug loading (%), size (nm), PDI, and zeta potential (mV), as shown in Table 3. Results indicated that higher chitosan percentages achieved greater drug loading but increased particle size beyond 700 nm. For instance, N8 exhibited the highest drug loading (30 %) but had a size of 3073 nm when using 2 % chitosan. Among the chitosan percentages tested, 0.5 % was found to provide optimal drug loading and small particle size for both LMW and MMW chitosan.

The crosslinker TPP demonstrated that higher percentages resulted in better drug loading and lower PDI, but significantly larger particle sizes. An intermediate concentration of 0.08 % TPP was determined to be optimal for both chitosan types.

Regarding the drug-to-polymer ratio, a 2:1 ratio generally yielded superior drug loading with smaller particle sizes and PDI compared to the 1:2 ratio and was thus considered optimal for both chitosan types. The TPP injection rate was optimized at 1 mL/min, which contributed to achieving smaller particle sizes.

Based on these characterizations, formulations N31 (LMW chitosan) and N35 (MMW chitosan) were selected for further studies and foam incorporation. These formulations, prepared with 0.5 % chitosan, 0.08

Table 3

Characterization results for 4-PBA loaded chitosan nanoparticles.

Chitosan Nanoparticle Batches	Average Drug Loading (%)	Size ± SD (nm)	PDI ± SD	Zeta Potential (mV) ± SD
N1	4.47	2503.33 ± 50.6	0.33	0.15 ± 0.1
N2	0.15	332.93 ± 38.41	0.57	-0.97 ± 0.8
N3	0.12	344.33 ± 30.4	0.55	-0.53 ± 0.1
N4	Did not form			
N5	0.13	268.00 ± 41.03	0.63	-0.27 ± 0.1
N6	3.44	359.80 ± 21.6	0.43	-1.71 ± 1.2
N7	0.66	415.40 ± 145	0.77	-0.19 ± 0.5
N8	30.14	3073.00 ± 369	0.27 ± 0.1	-1.15 ± 0.6
N9	14.76	809.17 ± 46	0.60	0.76 ± 1.3
N10	9.53	647.37 ± 12.1	0.57	-0.74 ± 1.1
N11	Did not form			
N12	0.24	816.33 ± 93.2	0.43 ± 0.1	0.32 ± 0.5
N13	0.16	536.27 ± 25.8	0.53	0.70 ± 0.7
N14	Did not form			
N15				
N16	0.38	528.50 ± 134	0.43	-7.10 ± 0.3
N17	Did not form			
N18	0.21	800.47 ± 51	0.57	-0.26 ± 2.9
N19	0.95	642.26 ± 32	0.50	7.09 ± 0.2
N20	0.86	663.00 ± 86	0.80	2.36 ± 1.8
N21	0.61	165.98 ± 89.6	1.00	37.53 ± 0.3
N22	1.06	3823.00 ± 368	1.00	5.13 ± 1.15
N23	0.14	1070.00 ± 164	0.80 ± 0.1	10.16 ± 0.16
N24	1.53	1848.00 ± 248	0.40 ± 0.2	7.99 ± 0.3
N25	0.29	570.00 ± 23.9	0.40	14.03 ± 0.05
N26	0.97	943.00 ± 107	1.00	6.29 ± 0.26
N27	0.60	1030.00 ± 112.4	0.30 ± 0.1	1.76 ± 4.4
N28	0.70	2228.00 ± 227.3	0.30	9.59 ± 0.05
N29	0.02	199.93 ± 48.7	0.90	-20.50 ± 1.15
N30	0.32	234.23 ± 9.4	0.63	-6.99 ± 1.7
N31	5.04	141.88 ± 26.3	0.20	-16.67 ± 1.15
N32	0.22	203.97 ± 44.3	0.90	-22.73 ± 1.6
N33	0.24	339.52 ± 251.1	0.50 ± 0.3	-21.60 ± 0.2
N34	0.44	131.50 ± 11	0.93	-37.57 ± 0.18
N35	10.09	176.10 ± 36	0.26	-19.37 ± 1.6
N36	0.47	211.23 ± 75	0.40	-1.79 ± 0.1
N37	0.04	241.80 ± 47	0.93	-0.69 ± 3.9
N38	0.04	434.43 ± 53	0.73 ± 0.1	-6.14 ± 5.5

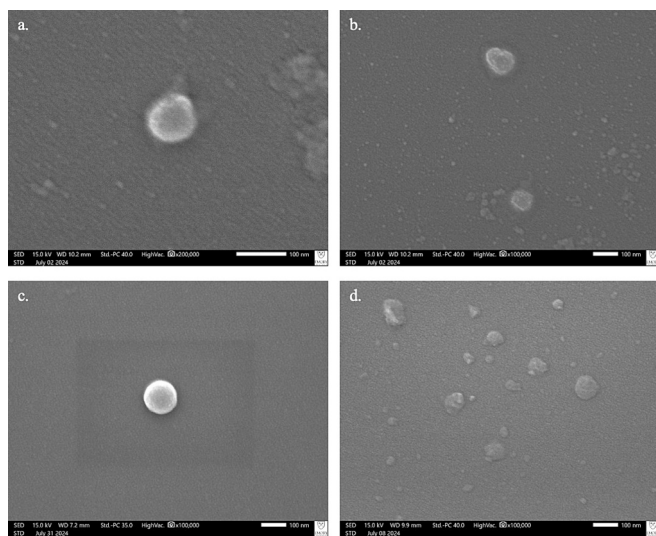


Fig. 1. (a, b) SEM image of N31 nanoparticles (c, d) SEM image of N35 nanoparticles.

% TPP, an injection rate of 1 mL/min, and a drug:polymer ratio of 2:1, exhibited the following characteristics:

N31 (LMW chitosan): Size of 141.88 ± 26.31 nm, drug loading of 5.04 %, entrapment efficiency of 93.85 %, PDI of 0.2, and zeta potential

of -16.67 mV.

N35 (MMW chitosan): Size of 176.1 ± 36.97 nm, drug loading of 10.09 %, entrapment efficiency of 93.57 %, PDI of 0.26, and zeta potential of -19.37 mV.

The PDI values (<0.3) indicate that the particles were monodisperse, while the negative zeta potentials suggest physical stability of the formulations. Generally, MMW chitosan demonstrated higher drug loading compared to LMW chitosan, albeit with slightly larger particle sizes.

It is worth noting that the zeta potential values (-16.67 mV and -19.37 mV) fall within the range of -15 to -30 mV, which is considered to provide moderate stability. This stability is due to electrostatic repulsion between particles, reducing the likelihood of aggregation. Additionally, the high entrapment efficiency (>93 %) for both formulations suggest efficient drug encapsulation within the chitosan nanoparticles, which is crucial for controlled-release applications.

3.2. SEM studies

The results of the SEM analysis showed uniform spherical nano-sized particles, indicating successful nanoparticle formation (Fig. 1). Most of the 4-PBA-loaded chitosan nanoparticles with both LMW and MMW chitosan showed a size of less than 100 nm.

3.3. Drug-polymer interaction using FTIR analysis

The FTIR spectra of 4-PBA, chitosan polymers (LMW and MMW), TPP, and the nanoparticle formulations (N31, N35) are presented in Fig. 2. Pure 4-PBA exhibited characteristic absorption bands at $3000\text{--}2800\text{ cm}^{-1}$ (aromatic and aliphatic C-H stretching) and a strong peak at approximately 1700 cm^{-1} corresponding to the carboxylic acid carbonyl stretching. Both chitosan varieties displayed broad bands at $3355\text{--}3400\text{ cm}^{-1}$ (O-H and N-H stretching vibrations), 2875 cm^{-1} (C-H stretching), $1653\text{--}1660\text{ cm}^{-1}$ (amide C=O stretching), and distinctive saccharide structure signals between $1150\text{--}1000\text{ cm}^{-1}$ (C-O-C stretching). TPP showed characteristic peaks at approximately 1215 cm^{-1} (P=O stretching) and 890 cm^{-1} (P-O-P asymmetric stretching). In the nanoparticle formulations N31 and N35, several significant shifts were observed: the 4-PBA carbonyl peak shifted from 1700 cm^{-1} to approximately 1630 cm^{-1} , suggesting interaction with chitosan's amino groups; the chitosan amino band at 1560 cm^{-1} decreased in intensity and shifted, indicating ionic cross-linking with TPP phosphate groups; and new absorption bands appeared at approximately $1220\text{--}1250\text{ cm}^{-1}$, attributable to P=O stretching of TPP following ionic gelation. Additionally, the broader peaks in the $3400\text{--}3200\text{ cm}^{-1}$ region for both nanoparticle formulations compared to pure components further confirm successful interactions between 4-PBA and chitosan, demonstrating effective nanoparticle formation through electrostatic and hydrogen bonding interactions.

3.4. DSC analysis

DSC thermograms provided critical insights into the thermal behavior and molecular interactions within the developed nanoparticle formulations, as shown in Fig. 3. The thermogram of pure 4-PBA revealed a characteristic sharp endothermic peak at 52°C , corresponding to its melting transition and confirmed its crystalline nature. In contrast, both low and medium-molecular-weight chitosan polymers exhibited more complex thermal profiles, featuring a broad endothermic event around 100°C (attributable to moisture evaporation) and a prominent exothermic peak between 200°C - 225°C (indicative of polymer degradation through depolymerization). Notably, the 4-PBA-loaded chitosan nanoparticle formulations (N31 and N35) demonstrated altered thermal behavior compared to their individual components. The absence of the distinct 4-PBA melting endotherm in both nanoparticle preparations suggest successful molecular dispersion of the drug within the polymeric matrix, resulting in a transition from the

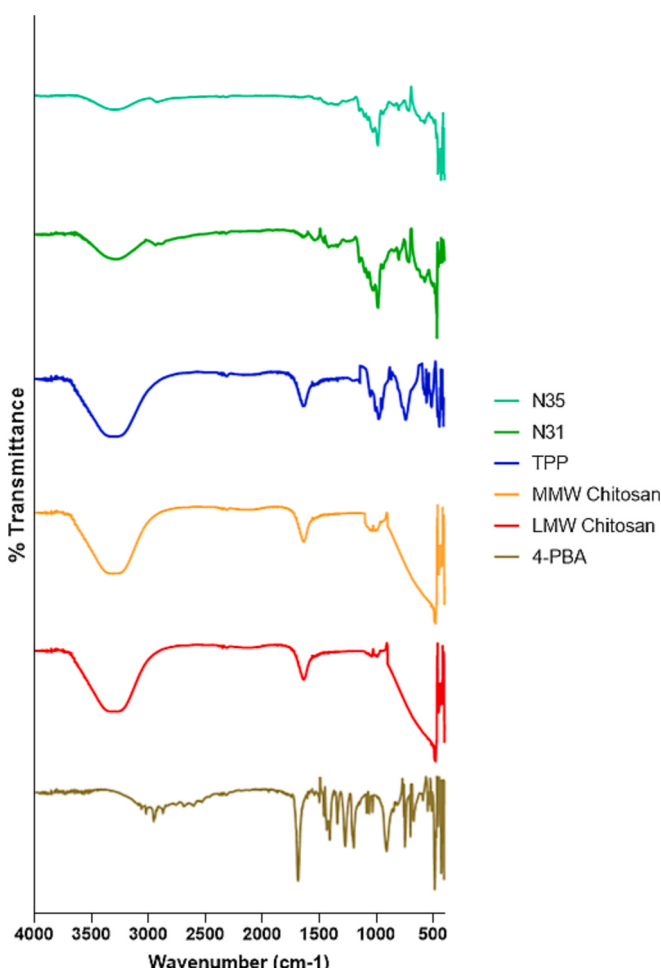


Fig. 2. FTIR spectra analyzed from the wavelength of 4000 to 500 cm^{-1} for 4-PBA, chitosan LMW and MMW polymer, TPP, N31 and N35.

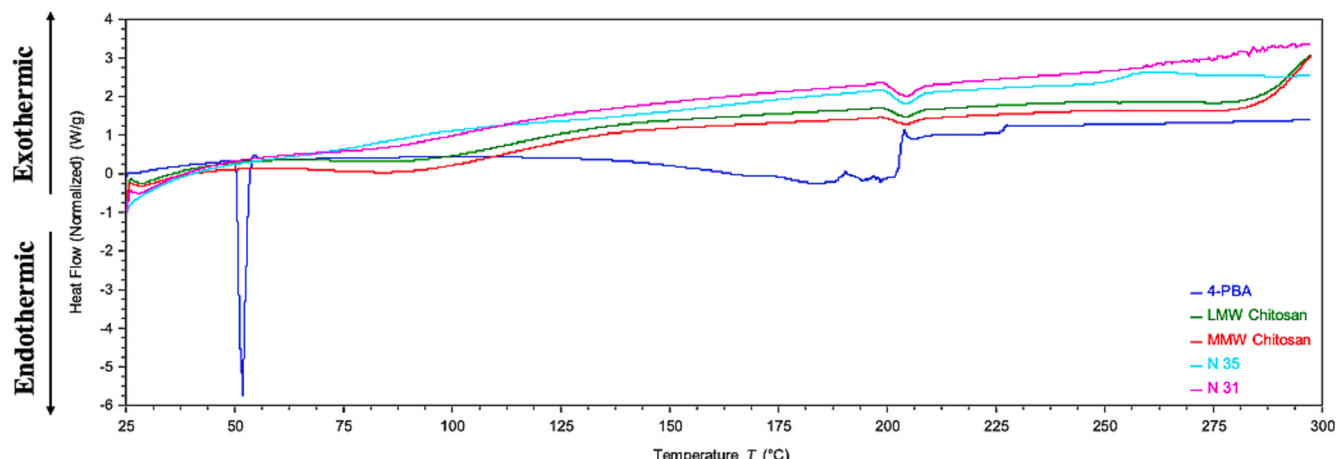


Fig. 3. Dsc thermograms of 4-PBA, chitosan (LMW and MMW), N31 and N35. Endothermic processes are indicated by downward peaks (↓).

crystalline to amorphous state. The preservation of modified chitosan-related thermal events in the nanoparticles, although with slight shifts in transition temperatures, confirms the structural integrity of the carrier system while indicating drug-polymer interactions at the molecular level. These thermal characteristics collectively support the effective encapsulation of 4-PBA within the chitosan nanoparticles, a crucial factor for enhanced drug solubility and controlled release properties.

3.5. Stability studies

The storage stability of N31 and N35 nanoparticles was evaluated under two conditions: accelerated degradation ($40^{\circ}\text{C} \pm 2^{\circ}\text{C}$, 75 % RH $\pm 5\%$) and accelerated refrigerated storage ($25^{\circ}\text{C} \pm 2^{\circ}\text{C}$, 60 % RH $\pm 5\%$), where all runs were considered for $n = 3$.

3.5.1. Drug loading and physical stability

After 30 days, nanoparticles stored at $25^{\circ}\text{C}/60\%$ RH retained their drug loading capacity without significant loss. In contrast, those exposed to $40^{\circ}\text{C}/75\%$ RH exhibited substantial drug leakage, with N31 losing 52 % and N35 losing 38 % of their loaded 4-PBA. HPLC analysis confirmed the chemical stability of 4-PBA, as no shifts in retention time were observed under either condition. Lyophilized nanoparticles maintained their white, free-flowing morphology without agglomeration, indicating robust physical stability. These findings highlight the formulation's resilience to moisture and temperature fluctuations, critical for long-term storage viability.

3.5.2. Particle size, polydispersity Index, and zeta potential

Both formulations displayed modest size increases after 30 days of storage, with temperature-dependent effects. Nanoparticles stored at accelerated conditions ($40^{\circ}\text{C}/75\%$ RH) exhibited more pronounced enlargement: N31 increased to 548.3 ± 90.2 nm and N35 to 306.8 ± 42.3 nm, both reaching a PDI of 0.5. Under milder conditions ($25^{\circ}\text{C}/60\%$ RH), the size expansion was more contained, with N31 measuring 446.5 ± 2.9 nm and N35 reaching 192.0 ± 25.2 nm, accompanied by PDI values of 0.4 and 0.6, respectively. This increase in size likely resulted from limited particle agglomeration during storage.

Surface charge stability was maintained across all storage conditions, with zeta potential values consistently ranging between -15 mV and -30 mV, indicating adequate electrostatic repulsion between particles. Notably, the MMW chitosan formulation (N35) demonstrated superior stability at lower temperatures, preserving both drug content (as discussed in section 3.5.1) and particle size characteristics. These findings suggest that refrigerated storage would be optimal for maintaining the physicochemical integrity of these nanoparticle systems over extended periods.

3.5.3. FTIR analysis for structural integrity

FTIR spectra of N31 and N35 nanoparticles after one month of storage under different conditions ($25^{\circ}\text{C}/60\%$ RH and $40^{\circ}\text{C}/75\%$ RH) are presented in Fig. 4. Both formulations maintained their characteristic spectral features regardless of storage conditions, indicating the preservation of chemical structure and stability of the drug-polymer interactions. The spectra exhibited typical absorption bands at $3400\text{--}3200\text{ cm}^{-1}$ (O-H and N-H stretching), $2920\text{--}2850\text{ cm}^{-1}$ (aliphatic C-H stretching), and $1650\text{--}1550\text{ cm}^{-1}$ (amide bands of chitosan and possible carboxylate interactions from 4-PBA). N31 demonstrated nearly identical spectral profiles under both storage conditions, with minimal variations in peak intensities. In contrast, N35 stored at $40^{\circ}\text{C}/75\%$ RH showed subtle changes in the relative intensities of peaks in the $1700\text{--}1500\text{ cm}^{-1}$ region compared to its $25^{\circ}\text{C}/60\%$ RH counterpart, potentially reflecting minor alterations in hydrogen bonding or ionic interactions. The fingerprint region ($1500\text{--}1000\text{ cm}^{-1}$) containing phosphate vibrations ($\text{P}=\text{O}$, $\text{P}-\text{O}$) remained largely unchanged, confirming the stability of the ionic crosslinking network.

3.5.4. DSC analysis for structural integrity

DSC analysis was conducted to assess the stability of N31 and N35 formulations stored under different conditions (60 % RH, 25°C and 75% RH, 40°C) for one month (Fig. 5). The thermograms revealed that N35 stored at 75 % RH, 40°C exhibited a partial reappearance of the 4-PBA melting peak ($\sim 52^{\circ}\text{C}$), suggesting recrystallization of the drug over time. This indicates that higher humidity and temperature conditions may lead to phase separation and reduce the stability of the amorphous drug-polymer system for MMW chitosan nanoparticles. In contrast, formulations stored at 60 % RH, 25°C retained their amorphous characteristics, demonstrating better stability under these conditions. Additionally, shifts in the chitosan endothermic peaks suggest potential moisture absorption and structural modifications in the polymer at elevated humidity levels. These findings highlight the importance of optimized storage conditions in maintaining the amorphous state of 4-PBA within chitosan-based formulations, which is crucial for preserving its enhanced solubility and bioavailability.

3.6. In-vitro drug release study (IVRT)

The in-vitro release profiles of 4-PBA from different formulations are presented in Fig. 6. The control formulation (4-PBA in foam F39) exhibited the highest cumulative release of 72.03 % over 24 h. The N35 nanoparticles incorporated in foam F39 demonstrated comparable efficacy, releasing 65.58 % of the encapsulated drug during the same period, while N31 in F39 foam showed significantly lower release at only 18.11 %. Both nanoparticle formulations displayed sustained-

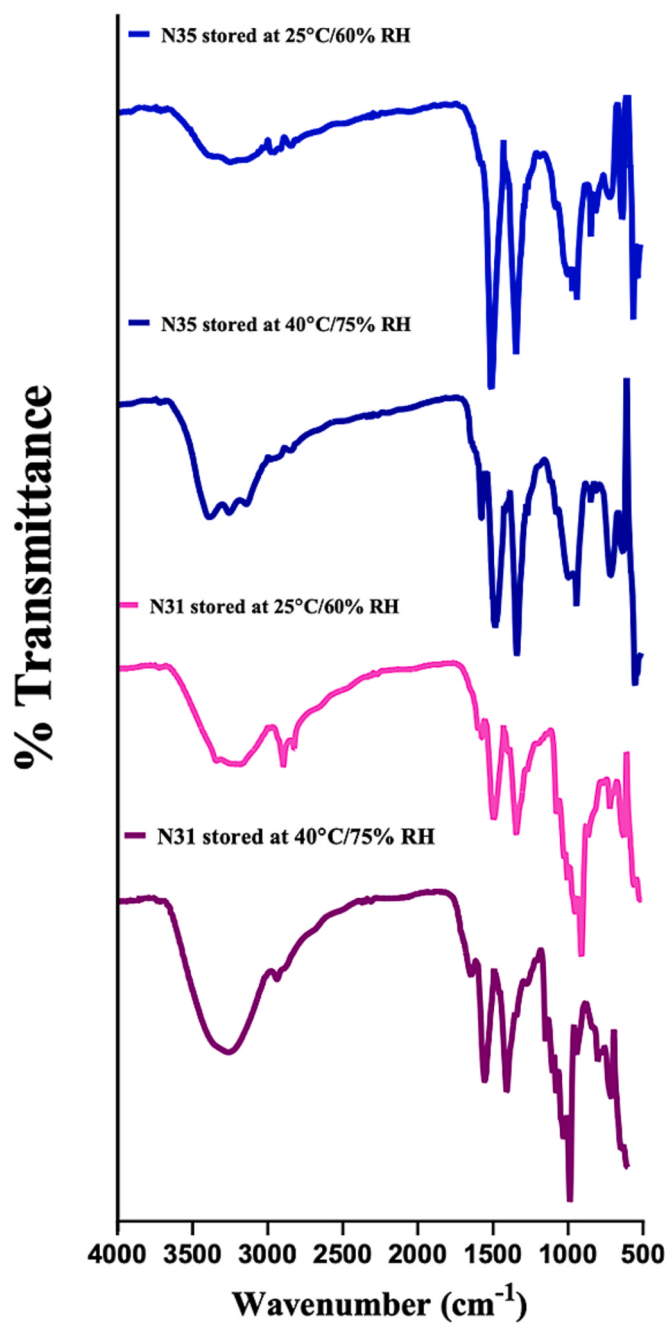


Fig. 4. FTIR spectra analyzed from the wavelength of 4000 to 500 cm^{-1} for N31 and N35 stored under different conditions ($25\text{ }^{\circ}\text{C}/60\text{ \% RH}$ and $40\text{ }^{\circ}\text{C}/75\text{ \% RH}$).

release characteristics, with N35 maintaining steady drug release for 8–10 h before reaching its plateau at 24 h. Notably, the total 4-PBA released from N35 was not significantly different from the control formulation, whereas N31 had substantial reduced drug release.

3.7. In-vitro permeation testing (IVPT)

3.7.1. IVPT to determine sustained delivery of 4-PBA from chitosan nanoparticles

The IVPT study revealed distinctive permeation profiles for 4-PBA across different formulations and vehicles (Fig. 7). The permeation profiles demonstrate clear formulation-dependent effects, with free 4-PBA exhibiting the highest permeation rate, followed by N35 and then

N31, which showed dramatically reduced permeation. At 24 h, free 4-PBA in foam F39 achieved the highest cumulative permeation ($348.10 \pm 5.37\text{ }\mu\text{g/cm}^2$), showing no statistically significant difference from the PBS control ($280.64 \pm 30.69\text{ }\mu\text{g/cm}^2$). This confirms that the foam vehicle itself does not significantly alter drug permeation kinetics. N35 in foam F39 demonstrated moderate permeation ($214.35 \pm 16.6\text{ }\mu\text{g/cm}^2$), representing a statistically significant reduction ($*p < 0.05$) compared to free 4-PBA, reducing 38.4 % of the free 4-PBA permeation. N31 in foam F39 exhibited the most pronounced reduction in permeation ($64.90 \pm 6.89\text{ }\mu\text{g/cm}^2$, *** $p < 0.001$), reducing 81.3 % when compared to the PBS control's free 4-PBA permeation. The time-course data further illustrate that both nanoparticle formulations provided sustained delivery patterns throughout the 24-hour period, with clearly differentiated profiles reflecting the influence of chitosan molecular weight on barrier properties and drug release kinetics.

3.7.2. IVPT using different skin types

The IVPT study comparing permeation across dermatomed porcine and human cadaver skin revealed consistent trends across formulations (Fig. 8). The amount of free 4-PBA delivered into the receptor chamber from foam F39 was similar between porcine ($354.65 \pm 2.13\text{ }\mu\text{g/cm}^2$) and human cadaver skin ($348.10 \pm 5.37\text{ }\mu\text{g/cm}^2$), with no statistically significant difference observed. Both nanoparticle formulations demonstrated reduced permeation compared to free 4-PBA, regardless of skin type. In porcine skin, N35 and N31 formulations decreased 4-PBA delivery by 54.7 % and 81.4 %, respectively, relative to the control in the foam vehicle. Specifically, the total cumulative delivery in porcine skin was $245.58 \pm 40.87\text{ }\mu\text{g/cm}^2$ for N35 and $101.23 \pm 20.14\text{ }\mu\text{g/cm}^2$ for N31. This reduction pattern was consistent with the results observed in human skin, where N35 consistently delivered more 4-PBA than N31 across the 24-hour study period. Statistical analysis confirmed no significant differences in permeation between skin types for any formulation, suggesting that both porcine and human skin models provided comparable barriers for these formulations. The permeation profiles further illustrated that free 4-PBA exhibited rapid delivery, while both nanoparticle formulations demonstrated sustained-release characteristics, with N35 achieving moderate sustained delivery and N31 showing the most pronounced reduction in overall permeation.

3.7.3. IVPT to determine decontamination efficiency

The efficiency of various foam formulations to decontaminate the skin of PAO is presented in Fig. 9. All tested formulations demonstrated decontamination efficiencies exceeding 50 %, with no significant reduction observed upon the addition of 4-PBA-loaded chitosan nanoparticles. The blank foam (F39) exhibited an efficiency of 73.47 %, while the foam containing free 4-PBA showed slightly lower efficiency (56.45 %), though this difference was not statistically significant ($p > 0.05$). Incorporating chitosan nanoparticles into the foam maintained comparable or improved decontamination performance, with N35-loaded foam achieving 70.04 % efficiency and N31-loaded foam exhibiting 88.59 %. Statistical analysis confirmed that adding nanoparticles to the foam did not compromise its decontamination properties, as both N31 and N35 formulations retained efficiencies above 70 %. These findings demonstrate that the therapeutic benefits of nanoparticle incorporation do not negatively impact the intrinsic decontamination efficiency of the foam vehicle, ensuring its dual functionality for drug delivery and effective decontamination.

3.7.4. IVPT to determine permeation of 4-PBA after lewisite (PAO) exposure to skin

To simulate real-world conditions, human cadaver skin was first exposed to PAO, followed by decontamination and subsequent application of the test formulations. The IVPT study demonstrated distinct permeation profiles of 4-PBA delivered via chitosan nanoparticles. After 24 h, the formulation containing N35 in foam F39 exhibited a cumulative permeation of $158.54 \pm 53.93\text{ }\mu\text{g/cm}^2$, whereas N31 in the same

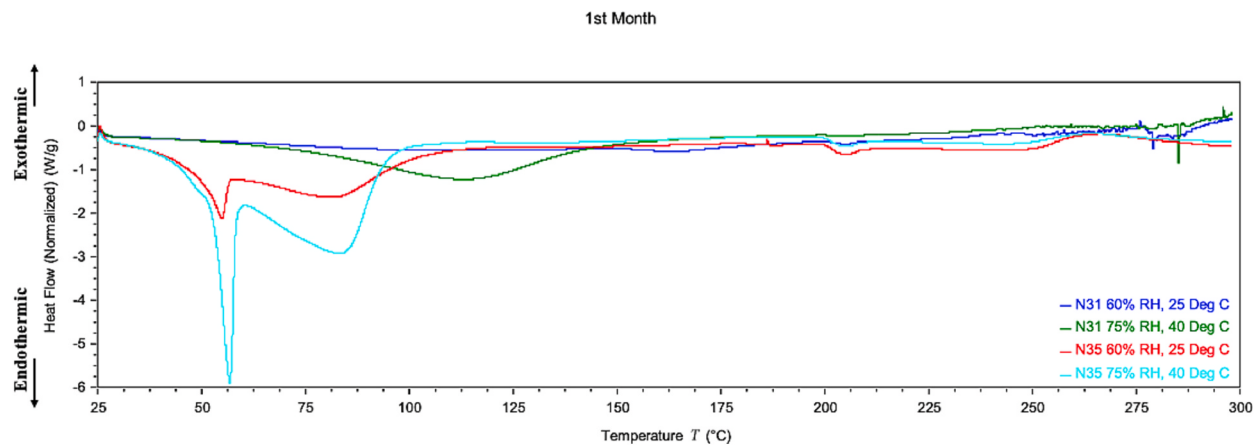
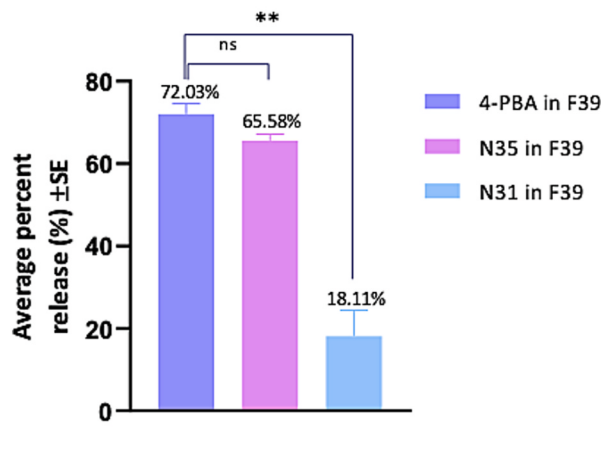


Fig. 5. Dsc thermograms of N31 and N35 stored at 60 % RH, 25 °C and 75 % RH, 40 °C for one month. Endothermic processes are indicated by downward peaks (↓).

a. Release of 4-PBA in 24hours



b. Release Profile of 4-PBA

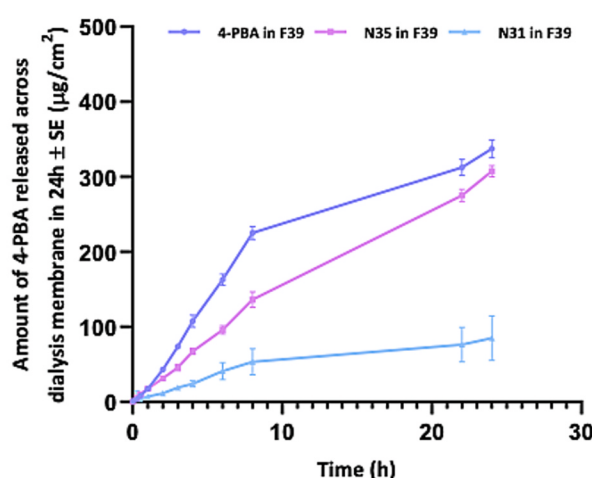
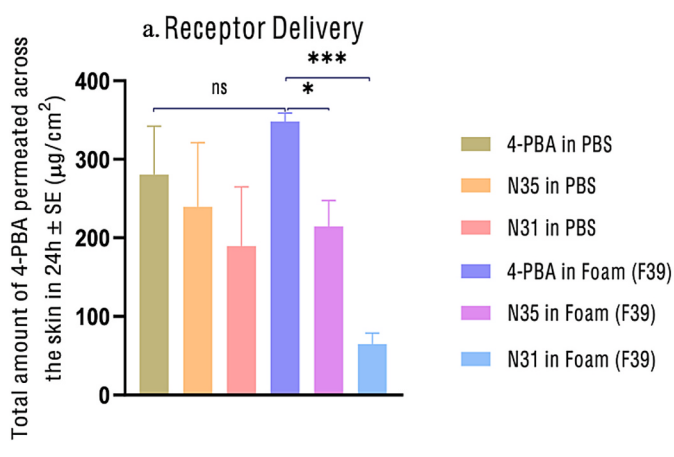


Fig. 6. (a,b) Results from In vitro release studies ($n = 4$); One-way ANOVA with Tukey's post hoc analysis; * ($p \leq 0.05$); *** ($p \leq 0.001$).



b. Permeation Profile of 4-PBA (Foam F39 as a vehicle)

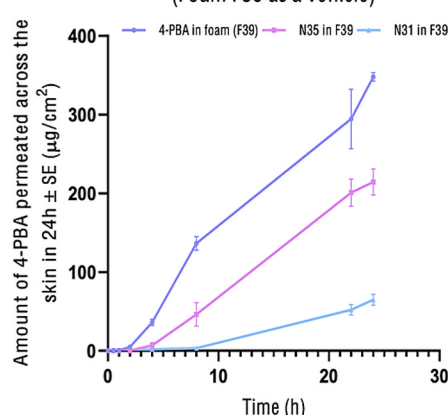


Fig. 7. (a, b) Results from IVPT studies ($n = 4$); One-way ANOVA with Tukey's post hoc analysis; * ($p \leq 0.05$); *** ($p \leq 0.001$), Permeation profile of 4-PBA through nanoparticles in Foam (F39).

foam base showed a slightly lower permeation of $138.25 \pm 14.72 \mu\text{g}/\text{cm}^2$. Both formulations displayed sustained release behavior, with N35 showing marginally higher permeation. These findings are consistent

with the results observed in uncompromised skin, as discussed in Section 3.7.1, indicating that the nanoparticle-foam system maintains effective delivery even under chemically challenged skin conditions.

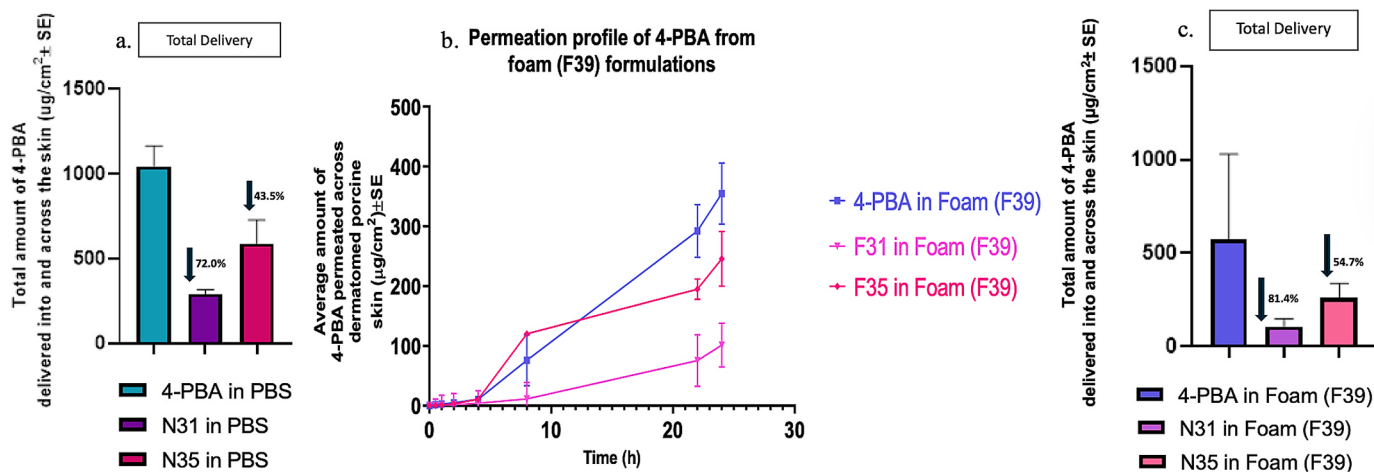


Fig. 8. A. total delivery of 4-pba from different formulations in pbs vehicle in dermatomed porcine skin; b. permeation profile of 4-pba from foam f39 formulations in dermatomed porcine skin; c. total delivery of 4-pba from different formulations in foam f39 vehicle in dermatomed porcine skin.

Decontamination Efficiency (%)

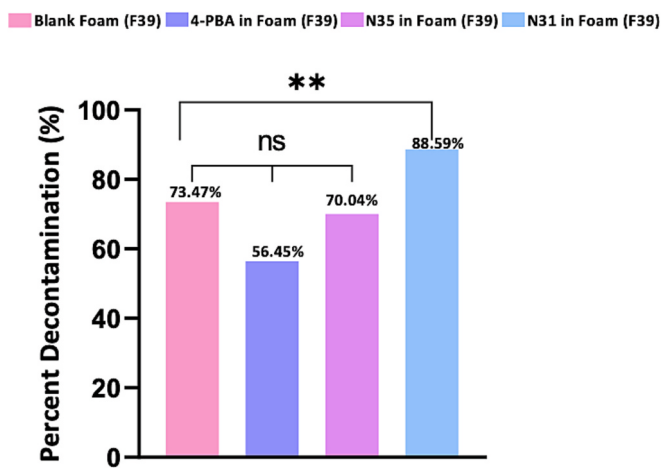


Fig. 9. Results from Decontamination studies ($n = 4$); One-way ANOVA with Tukey's post hoc analysis; * ($p \leq 0.05$); *** ($p \leq 0.001$).

Table 4

Lag time of 4-PBA delivery from chitosan nanoparticle formulations.

Formulations	Average (h)	SE
4-PBA in 1X PBS	0.93	0.27
4-PBA in Foam F39	2.25	0.89
N35 in PBS	6.91	0.15
N35 in F39	4.89	0.7
N31 in PBS	5.12	0.83
N31 in F39	7.9	0.94

3.8. Lag time calculation

The lag time of 4-PBA delivery varied significantly across different formulations and vehicles (Table 4). Free 4-PBA in PBS exhibited the shortest lag time (0.93 ± 0.27 h), serving as the baseline for comparison. When formulated in foam F39, free 4-PBA demonstrated an increased lag time (2.25 ± 0.89 h), suggesting vehicle-dependent effects on initial permeation. Encapsulation in chitosan nanoparticles substantially prolonged the lag times across all formulations. N35 nanoparticles showed differential behavior between vehicles, with PBS formulations yielding longer lag times (6.91 ± 0.15 h) compared to foam F39 (4.89 ± 0.70 h).

Notably, N31 formulations exhibited the most pronounced delay in initial drug delivery, with lag times of 5.12 ± 0.83 h in PBS and 7.90 ± 0.94 h in foam F39. The substantial extension of lag time for nanoparticle formulations, particularly N31 in foam F39 (approximately 8.5-fold increase compared to free 4-PBA in PBS), confirms the sustained-release characteristics of the chitosan matrix.

3.9. Topical application of foam formulated 4-PBA N35 + NAC protects against PAO-induced skin injury and inflammation in Ptch1^{+/−}/SKH-1 mice

In earlier study, we have demonstrated an enhanced transdermal delivery of 4-PBA and NAC and shown the safety and effectiveness of these drug agents against skin injury caused by PAO or lewisite (Dandekar et al., 2023; Srivastava et al., 2018).

Here, we test the efficacy of a novel formulation containing 4-PBA loaded in chitosan nanoparticle (N35) and dispensed in F39 foam formulation containing NAC as an antioxidant (4-PBA N35 + NAC) against PAO-induced skin inflammatory and tissue damaging responses at 24 hr time-point. PAO is a surrogate chemical of lewisite. Earlier, we demonstrated its utility for evaluating various drug candidates against lewisite in laboratory conditions (Srivastava et al., 2021; Srivastava et al., 2020). Our data demonstrate that topically application of 4-PBA N35 + NAC significantly diminished PAO-induced gross skin injury as observed by reduced erythema, edema and pinpoint-necrotic lesions in the exposed area (red circle, Fig. 10A). These effects were quantitatively scored and represented by Draize score. We observed that 4-PBA N35 + NAC treatment, but not placebo, significantly reduced PAO-induced Draize score (Fig. 10B). Analysis of H&E skin sections of PAO challenged animals revealed the presence of high number of immune cells infiltration and formation of microvesicant (mv), due to separation of epidermal and dermal layers of mouse skin (Fig. 10C). However, in 4-PBA N35 + NAC treated animals, the infiltration of immune cells as well as presence of mv structure in the skin were significantly less prominent (Fig. 10C and D). It is important to note that, though placebo treatment did not show any significant effects in lowering PAO-induced immune cell infiltration, it manifested some protective effects in mv formation. Thus, a reduced epidermal/dermal separation was recorded (Fig. 10D). Next, we assessed the effects of 4-PBA N35 + NAC on PAO-induced epidermal cell apoptosis. Both TUNEL staining and cleaved caspase-3 in the skin lysates were assessed. TUNEL stained skin sections showed significant reduced number of green positive epidermal apoptotic cells in 4-PBA N35 + NAC treated animals as compared to PAO and PAO + Placebo treatment groups (Fig. 10E). Similar effects were observed when we analyzed the western blot data for cleaved caspase-3,

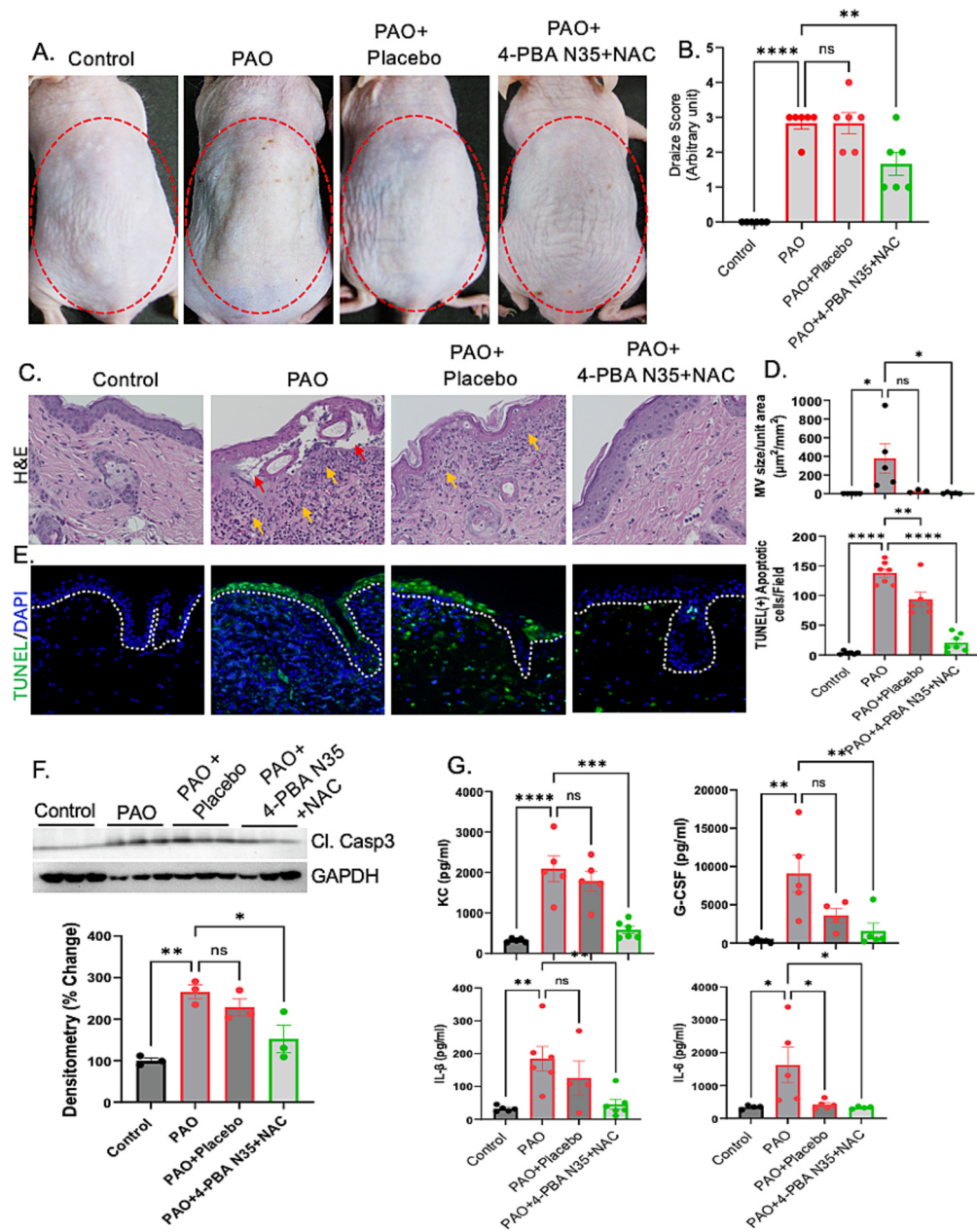


Fig. 10. Effects of foam formulated, 4-PBA N35 + NAC against PAO-induced skin injury in mice. (A) Representative mice photographs showing attenuation of PAO-induced skin injury by topical treatment of foam formulated, 4-PBA N35 + NAC, while placebo treatment did not show significant change compared to PAO exposed skin. Red circle indicates exposed area by various treatment groups. (B) Bar graph showing gross skin injury and was calculated based on Draize score (combine effects of erythema, edema and necrosis). (C & D) H&E-stained skin sections shows PAO-induced infiltration of inflammatory cells (red arrows) and microvesicant (mv) formation (yellow arrows), which was significantly reduced by treatment of foam formulated 4-PBA N35 + NAC in the skin. Placebo treatment did not show significant changes compared to PAO-induced immune cell infiltration, but manifested some protective effects in mv formation. (E) Representative microphotographs showing PAO-induced green TUNEL-positive apoptotic epidermal cells and protection by foam formulated 4-PBA N35 + NAC. Histogram showing quantitative analysis of the apoptotic cells in skin epidermis. (F) Western blot analysis of cleaved caspase-3 in the skin lysates of indicative treatment groups. GAPDH was used as endogenous control. Histogram showing quantitative analysis of band intensity in % change after normalization with GAPDH. (G) Cytokine analysis by protein multiplex. foam formulated 4-PBA N35 + NAC significant lower the production of PAO-induced inflammatory modulators G-CSF, KC, IL-6 and IL-1 β . $p < 0.05^*$, $p < 0.01^{**}$, $p < 0.001^{***}$, $p < 0.0001^{****}$ showed significance. ns-Non significance.

an apoptosis marker protein (Fig. 10F). Next, we assessed the effects of 4-PBA N35 + NAC on PAO-induced inflammatory mediators using protein multiplex cytokine analysis. As shown in Fig. 10G, following treatment with formulated 4-PBA N35 + NAC, we observed a significant diminution in the protein level of PAO-induced G-CSF, KC, IL-1 β , IL-6. However, placebo treatment did not show such effects, except for reducing PAO-induced IL-6. These data suggest that the topical treatment of formulated drug 4-PBA nanoparticle + NAC significantly

attenuates PAO-induced skin injury and inflammatory modulators.

3.10. Topical application of foam formulated 4-PBA N35 + NAC protects against PAO-induced UPR signaling in mice skin

Previously, we have demonstrated that the chemical chaperone, 4-PBA, block arsenical-mediated ER stress and associated UPR signaling in the skin keratinocytes both in vitro and in vivo (Li et al., 2016;

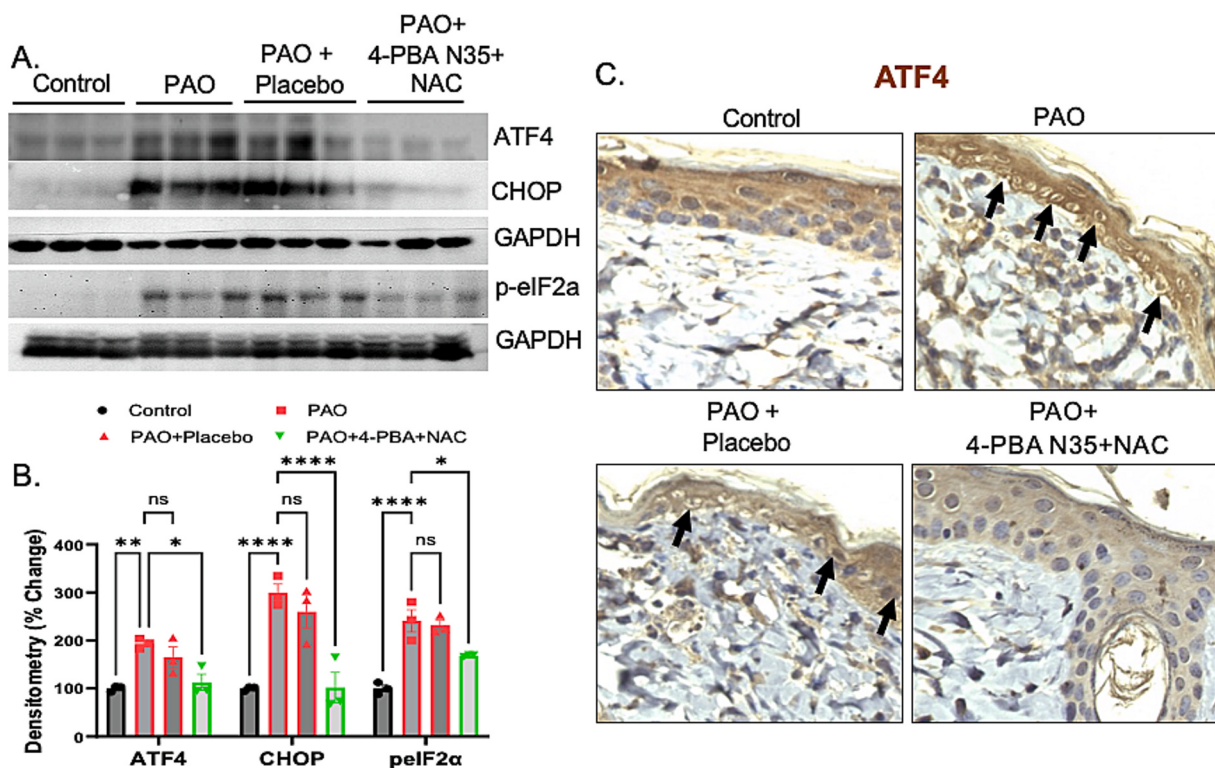


Fig. 11. Effects of foam formulated, 4-PBA N35 + NAC against PAO-induced unfolded protein response signaling pathway. (A) Western blot analysis of skin lysates showing expression of UPR signaling proteins ATF4, CHOP and p-eIF2 α in indicated treatments. GAPDH was used for endogenous control. Foam formulated 4-PBA N35 + NAC show significant reduction in PAO-induced ATF4, CHOP and p-eIF2 α , while placebo treatment does not have any effects on PAO-induced expression of these proteins. (B) Densitometry analysis of band intensity measured by Image J software and presented in % change. N = 3. (C) Immunohistochemistry analysis of ATF4 in skin epidermal cells of indicated treatment groups. Black arrows shows nuclear translocation and high expression of ATF4 in PAO and placebo-exposed skin epidermal cells. However, foam formulated 4-PBA N35 + NAC significantly reduced PAO-induced expression and nuclear appearance of ATF4 in skin cells. $p < 0.05^*$, $p < 0.01^{**}$, $p < 0.0001^{****}$ showed significance. ns-Non significance.

Srivastava et al., 2016). Here, we further tested whether our formulated drug 4-PBA N35 + NAC acts via similar mechanism of protection and can ameliorate PAO-induced UPR signaling. Our data demonstrate that 4-PBA N35 + NAC formulated drug significantly reduced expression of PAO-induced activation of UPR signaling proteins ATF4, CHOP and p-eIF2 α (Fig. 11 A and B). However, placebo did not have any noticeable changes in this regard. These data indicate that our formulated drug acts through downregulating ER stress associated UPR signaling axis and does not alter the mechanism of action of 4-PBA. We confirmed these results by IHC staining by recognizing the nuclear localization of ATF4 in PAO and PAO + Placebo, treated skin sections. As observed in western blot analysis, PAO-induced expression and nuclear translocation of ATF4 was significantly reduced (Fig. 11C).

4. Discussion

The need for novel antidote formulations against Lewisite skin injury was addressed by exploring 4-PBA as a potential therapeutic agent. Lewisite exposure was known to cause immediate burning sensations, followed by erythema and vesication within hours (Li et al., 2016; Kshirsagar et al., 2024). Although prompt decontamination was required, it was recognized that a sustained drug delivery system for 4-PBA could help mitigate the delayed manifestations of injury (Alkholief et al., 2023; Decontamination_of_Chemical_Wa, n.d.). Various transdermal delivery approaches, including chemical enhancers and physical methods such as microneedles and iontophoresis, were previously investigated to improve drug delivery (Dandekar et al., 2023; Vora et al., 2022; Kshirsagar et al., 2023). However, due to the inherently high transdermal permeation of 4-PBA, attributed to its moderate lipophilicity and low molecular weight, encapsulation into micro-

nanoparticles was identified as the most rational strategy to achieve prolonged and controlled release for extended therapeutic benefit (Bhattacharjee et al., 2025; Kshirsagar et al., 2024). This study developed a dual-action foam by incorporating 4-PBA-loaded nanoparticles, enabling simultaneous decontamination and prolonged antidote delivery to better address both immediate and delayed effects of Lewisite exposure.

4-PBA-loaded chitosan nanoparticles were formulated using the ionic gelation method with chitosan as the encapsulating polymer and TPP as the crosslinking agent. Chitosan, a natural polysaccharide derived from chitin, is biocompatible, biodegradable, and possesses mucoadhesive properties, making it an ideal candidate for controlled drug delivery applications. The ionic gelation technique was selected due to its mild preparation conditions without toxic solvents, simple execution, and cost-effectiveness. This method relies on the electrostatic interaction between positively charged amino groups of chitosan ($R-NH_3^+$) and negatively charged phosphate groups of TPP, leading to spontaneous nanoparticle formation under controlled stirring conditions (Ma et al., 2022; Hussain et al., 2014).

The formulation of 4-PBA-loaded chitosan nanoparticles via ionic gelation was systematically optimized by evaluating critical parameters influencing nanoparticle characteristics. Chitosan concentration and molecular weight were found to profoundly impact drug loading and particle size. Higher chitosan concentrations (e.g., 2 %) increased drug loading but resulted in excessively large particles (>700 nm), consistent with previous reports linking chitosan's viscosity and chain entanglement to nanoparticle growth. MMW chitosan demonstrated superior drug loading (10.09 %) compared to LMW chitosan (5.04 %), likely due to its longer polymer chains providing more binding sites for 4-PBA (Al-Kassas et al., 2016; Nair et al., 2019).

The crosslinker TPP concentration and injection rate were optimized to balance stability and particle size (Hasanovic et al., 2009). A TPP concentration of 0.08 % minimized PDI (<0.3) while maintaining nanoscale dimensions, aligning with studies showing that moderate crosslinking enhances structural integrity without excessive aggregation. The drug-to-polymer ratio (2:1) yielded optimal loading and particle characteristics, contrasting conventional systems where higher polymer ratios typically dominate. This deviation may arise from 4-PBA's moderate lipophilicity ($\log P \sim 2.2$), which facilitates electrostatic and hydrogen-bonding interactions with chitosan. Literature suggests drugs with moderate lipophilicity ($\log P$ 2–3) often exhibit balanced solubility in both aqueous and lipid phases, which can facilitate interactions with chitosan's hydrophilic (amino/hydroxyl groups) and hydrophobic regions (Herdiana et al., 2024).

The selected formulations, N31 (LMW) and N35 (MMW), exhibited monodisperse distributions ($PDI < 0.3$) and moderate stability (zeta potential: -16.67 to -19.37 mV), attributed to electrostatic repulsion between negatively charged particles. Remarkably high entrapment efficiency (>93 %) highlighted the ionic gelation method's efficacy in encapsulating 4-PBA, critical for sustained release.

The SEM analysis revealed uniform spherical nano-sized particles, confirming successful nanoparticle formation through ionic gelation (Fig. 1). Both LMW and MMW chitosan-based formulations exhibited particle sizes below 100 nm. This size distribution is consistent with previous reports on chitosan-TPP nanoparticles prepared under optimized conditions, where controlled ionic crosslinking produces discrete nanostructures (Al-Kassas et al., 2016; Hasanovic et al., 2009; Matos et al., 2015). The spherical morphology can be attributed to the mechanism of nanoparticle formation, wherein electrostatic interactions between positively charged chitosan and negatively charged TPP lead to spontaneous gelation under controlled stirring conditions, resulting in uniform particle architecture (Hasanovic et al., 2009; Phatale et al., 2022).

FTIR spectroscopic analysis (Fig. 2) provided insights into the molecular interactions between 4-PBA, chitosan, and TPP within the nanoparticle matrix. In the nanoparticle formulations N31 and N35, significant spectral shifts were observed, notably the displacement of 4-PBA's carbonyl peak from 1700 cm^{-1} to approximately 1630 cm^{-1} , suggesting interaction with chitosan's amino groups. Additionally, the chitosan amino band at 1560 cm^{-1} decreased in intensity and shifted, indicating ionic crosslinking with TPP phosphate groups. The appearance of new absorption bands at $1220\text{--}1250\text{ cm}^{-1}$, attributable to P=O stretching following ionic gelation, further confirmed successful nanoparticle formation. The broader peaks observed in the $3400\text{--}3200\text{ cm}^{-1}$ region for both nanoparticle formulations, compared to their individual components, suggest extensive hydrogen bonding networks within the nanoparticle structure. These spectral modifications collectively demonstrate the successful incorporation of 4-PBA within the chitosan-TPP matrix through both electrostatic and hydrogen bonding interactions. Similar spectral shifts have been reported in the literature previously for drug-loaded chitosan nanoparticles, where carbonyl peak shifts indicated drug entrapment within the polymer network. The retention of all major characteristic peaks, though with shifts in wave-number or intensity, confirms the physical entrapment of 4-PBA without chemical degradation, essential for maintaining drug stability and therapeutic efficacy (Szymańska and Winnicka, 2015; Kumar Jangid et al., 2023; Ahmed et al., 2024).

The observed nano-scale dimensions and spectroscopic evidence of successful molecular interactions suggest that the ionic gelation method effectively produced stable 4-PBA-loaded chitosan nanoparticles with preserved drug integrity. These findings are consistent with previous studies on chitosan-based nanocarriers, where similar morphological and spectroscopic characteristics were associated with high encapsulation efficiency and controlled release properties (Alkholief et al., 2023; Al-Kassas et al., 2016; Ahmed et al., 2024).

This spectroscopic evidence was supported by stability studies

conducted at $25\text{ }^{\circ}\text{C}/60\text{ \% RH} \pm 5\text{ \%}$ for one month, where no significant decrease in drug content was observed for either N31 or N35 formulations, as determined by validated HPLC analysis. Importantly, the chromatographic retention time of 4-PBA remained unchanged throughout the study period, providing quantitative evidence against chemical modification of the encapsulated drug. The stability of these chitosan nanoparticles can be attributed to the ionic crosslinking network formed with TPP, which creates a protective matrix around the drug molecules. Literature indicates that chitosan nanoparticles can maintain their structural integrity at temperatures up to $80\text{ }^{\circ}\text{C}$, with endothermic transitions typically occurring above $135\text{ }^{\circ}\text{C}$ (Ma et al., 2022; Kumar et al., 2023). The moderate negative zeta potential values (-16 to -30 mV) further contributed to physical stability by preventing particle aggregation through electrostatic repulsion. These findings collectively demonstrate that the ionic gelation method produces 4-PBA-loaded chitosan nanoparticles with excellent chemical stability under standard storage conditions, though accelerated conditions ($40\text{ }^{\circ}\text{C}/75\text{ \% RH}$) did induce some physical changes and drug leakage as discussed previously.

Foam F39 was employed in this study as a multifunctional vehicle for the delivery of 4-PBA-loaded chitosan nanoparticles, offering both effective decontamination and enhanced drug delivery (Vora et al., 2022; Kumar et al., 2022). The formulation was specifically optimized by replacing SLES with Tween 20, to improve safety and regulatory compliance while maintaining robust foaming capacity and skin compatibility. Tween 20's ability to lower surface tension facilitated the formation of a stable and uniform foam structure, which is essential for even application and coverage of the skin surface. The inclusion of ethanol and propylene glycol served dual roles: ethanol enhanced antimicrobial properties and solubilized 4-PBA, while propylene glycol contributed to foam stability and reduced evaporation, ensuring prolonged contact with the skin. Oleic acid was incorporated as a permeation enhancer, known to disrupt stratum corneum lipids and facilitate transdermal drug absorption. The careful balance of these excipients resulted in a foam that was easy to spread and showed a decontamination efficiency exceeding 70 % across all tested formulations. Importantly, the integration of lyophilized chitosan nanoparticles (delivering 1.5 mg 4-PBA per mL) did not compromise the foam's stability or its ability to remove chemical contaminants. This approach aligns with literature highlighting the utility of foam-based vehicles for both wound care and topical drug delivery, where the combination of effective cleansing, moisture retention, and controlled drug release is highly advantageous. By leveraging these properties, foam F39 provided a novel dual-action platform for simultaneous decontamination and sustained antidote delivery, representing a significant advance in the management of chemical warfare-induced skin injuries.

The in vitro release profiles of 4-PBA from various formulations revealed distinct release patterns governed by matrix composition and polymer characteristics. The control formulation (free 4-PBA in foam F39) exhibited rapid release kinetics with over 70 % cumulative release within 24 h, consistent with the unrestricted diffusion of solubilized drug molecules. In contrast, both nanoparticle formulations demonstrated modified release profiles, although with substantial differences between them. The superior release from N35 (MMW chitosan, 65.58 %) compared to N31 (LMW chitosan, 18.11 %) can be attributed to the influence of polymer molecular weight on drug-polymer interactions and matrix density. MMW chitosan likely forms a matrix with optimal porosity that maintains sufficient drug solubility while allowing controlled diffusion, whereas the tighter network formed by LMW chitosan may excessively restrict drug movement. The observed release profiles align with previous reports on chitosan nanoparticles, where drug release rates are influenced by multiple factors, including polymer concentration, crosslinking density, and molecular weight (Alkholief et al., 2023; Şenyigit et al., 2010). The N35 formulation demonstrated an optimal balance between sustained delivery and total drug release, making it potentially more suitable for therapeutic applications

requiring both immediate and prolonged drug exposure. The substantially lower release from N31 suggests its potential utility in applications demanding extended release over longer periods, though dose adjustment may be necessary to achieve therapeutic concentrations.

The IVPT studies conducted on dermatomed human skin revealed significantly reduced permeation of 4-PBA from chitosan nanoparticle formulations compared to the control group, correlating with controlled release profiles observed in the IVRT studies. Both N35 (MMW chitosan) and N31 (LMW chitosan) demonstrated sustained delivery patterns, with N35 reducing 38.4 % while N31 reducing 81.3 % of 4-PBA permeation in the control group. This differential permeation can be attributed to molecular weight-dependent barrier properties, where LMW chitosan (N31) forms a denser matrix that more effectively restricts drug diffusion compared to MMW chitosan (N35) (Ma et al., 2022; Abdel-Hafez et al., 2018). The vehicle effect was minimal, as evidenced by similar permeation between PBS and foam formulations, suggesting that drug release from the nanoparticles, rather than vehicle-skin interactions, primarily controlled permeation kinetics. The lag time calculations further substantiated these findings, with nanoparticle formulations showing 5–8 fold increases in lag time compared to free 4-PBA, confirming their sustained-release functionality. Importantly, these permeation patterns remained consistent across both human and porcine skin models, validating the robustness of these findings across different biological membranes. Nanoparticles cannot readily penetrate the stratum corneum due to their size, instead functioning as drug reservoirs that release 4-PBA gradually over extended periods, potentially reducing irritation potential while improving therapeutic efficacy (Herdiana et al., 2024; Kshirsagar et al., 2024). Notably, even after PAO exposure, which typically compromises skin barrier function, the nanoparticle formulations maintained their controlled delivery profiles, suggesting that these systems would remain effective under real-world chemical exposure scenarios. The preservation of decontamination efficiency alongside sustained drug delivery represents a significant advantage of these formulations, offering dual functionality critical for chemical injury management. This approach provides proof-of-concept for a formulation technique to sustain delivery of 4-PBA at the site of potential Lewisite-mediated injury in human skin.

In our in vivo studies, PAO consistently produced characteristic vesicant injury in the Ptch1^{+/−}/SKH-1 mouse model, manifesting as erythema, edema, and epidermal-dermal separation. Treatment with 4-PBA loaded in chitosan nanoparticles (N35) combined with NAC significantly mitigated these effects. NAC was added to the formulation for its potent antioxidant properties, which help neutralize ROS generated by Lewisite exposure, thereby reducing oxidative stress, inflammation, and promoting wound healing in the skin (Kshirsagar et al., 2023). Consistent with 4-PBA's established mechanism as a chemical chaperone, our formulation significantly reduced PAO-induced inflammatory mediators, including G-CSF, KC, IL-1 β , and IL-6. These results demonstrate that nanoparticle encapsulation maintains 4-PBA's fundamental protective mechanisms against vesicant injury through suppression of ER stress-induced inflammation and apoptosis, while potentially enhancing its local efficacy through sustained delivery at the injury site.

The results from both in vitro and in vivo evaluations indicate that 4-PBA-loaded chitosan nanoparticles hold promise for protecting skin against arsenical-induced injury. These findings support further research focused on dose optimization and also explore integrating a chemical indicator system into the formulation, enabling rapid identification of chemical exposure, effective decontamination, and sustained antidote delivery. Such a multifunctional system could significantly improve emergency first-line treatment for Lewisite and similar chemical injuries.

5. Conclusion

Chitosan nanoparticle formulations loaded with 4-PBA were

successfully developed using ionic gelation, with systematic optimization of chitosan molecular weight, crosslinker (TPP) concentration, drug-polymer ratio, and injection rate. The optimized formulations, N31 (LMW chitosan) and N35 (MMW chitosan), exhibited nanoscale particle sizes (141–176 nm), high entrapment efficiency (>93 %), and monodisperse distributions (PDI < 0.3), while maintaining moderate stability (zeta potential: −16.67 to −19.37 mV). *In-vitro*, release and permeation studies demonstrated sustained drug delivery over 24 h, with N35 and N31 achieving 65.58 % and 18.11 % of 4-PBA release, and 38.4 % and 81.3 % reduced permeation efficiency, respectively, relative to free 4-PBA in 24 h. Critically, nanoparticle incorporation into foam F39 preserved decontamination efficacy (>70 %) while enabling prolonged antidote delivery, even in PAO-compromised skin. Furthermore, *in vivo* studies demonstrated that the optimized formulation containing N35 chitosan nanoparticles combined with NAC provided significant protection against PAO-induced skin injury and suppressed inflammatory cytokine production in Ptch1^{+/−}/SKH-1 hairless mice. Importantly, we confirmed that the formulated 4-PBA retained its mechanism of action, acting through the UPR signaling pathway, similar to the unformulated drug.

These findings validate the translational potential of chitosan nanoparticle-loaded foam as a dual-action system (both decontamination and delivery) for arsenical-mediated skin injury management.

6. Statements and declarations

6.2. Consent for publication

The authors have read the manuscript and given their consent for publication.

CRediT authorship contribution statement

Meheli Ghosh: Writing – review & editing, Writing – original draft, Visualization, Validation, Methodology, Investigation, Formal analysis, Conceptualization. **Nethra Viswaroopan:** Methodology, Investigation. **Sharvari M. Kshirsagar:** Methodology, Investigation. **Jasim Khan:** Validation. **Suha Mohiuddin:** Validation. **Ritesh K. Srivastava:** Writing – review & editing, Validation, Formal analysis. **Mohammad Athar:** Supervision, Project administration, Funding acquisition, Conceptualization. **Ajay K. Banga:** Supervision, Project administration, Conceptualization.

6.1. Ethics approval and consent to participate

Not applicable.

Funding

This project was supported by NIH/NIAMS U01AR078544 to M.A. The sponsors had no involvement in the design of the study, data collection, analysis or interpretation, manuscript writing, or publication.

Declaration of competing interest

The authors declare that they have no known competing financial interests or personal relationships that could have appeared to influence the work reported in this paper.

Acknowledgments

The authors would like to thank the NIH/NIAMS for funding this project (U01AR078544). The authors would like to acknowledge the Emory University Robert P. Apkarian Integrated Electron Microscopy Core Facility (RRID: SCR_023537) for conducting the Scanning Electron

Microscopy analysis.

Data availability

Data will be made available on request.

References:

- Srivastava, R.K., Li, C., Weng, Z., Agarwal, A., Elmets, C.A., Afaq, F., Athar, M., 2016. Defining cutaneous molecular pathobiology of arsenicals using phenylarsine oxide as a prototype. *Sci. Rep.* 6. <https://doi.org/10.1038/srep34865>.
- Karalliedde, L., Wheeler, H., Maclehole, R., Murray, V., 2000. Possible immediate and long-term health effects following exposure to chemical warfare agents. *Public Health* 114, 238–248. <https://doi.org/10.1038/sj.ph.1900659>.
- Li, C., Srivastava, R.K., Weng, Z., Croutch, C.R., Agarwal, A., Elmets, C.A., Afaq, F., Athar, M., 2016. Molecular mechanism underlying pathogenesis of lewisite-induced cutaneous blistering and inflammation: chemical chaperones as potential novel antidotes. *Am. J. Pathol.* 186 (10), 2637–2649. <https://doi.org/10.1016/j.apath.2016.06.012>.
- Acute Exposure Guideline Levels for Selected Airborne Chemicals, 2016. National Academies Press. Doi: 10.17226/23634.
- Meenu, K., Kumar, N., Tiwari, K.R., Yadav, T., Tomar, R., Gupta, A.K., 2020. Synthesis and characterization of zeolite Linde Type W and its metal oxide composite Ag-O-LTW used for the decontamination of chemical warfare agent simulant. *Phosphorus Sulfur Silicon Relat. Elem.* 195 (10), 881–888. <https://doi.org/10.1080/10426507.2020.1762193>.
- Peters, R.A., Stocken, L.A., Thompson, R.H.S., 1945. British Anti-Lewisite (BAL). *Nature* 156 (3969), 616–619. <https://doi.org/10.1038/156616a0>.
- Peters, R.A., 1948. Development and theoretical significance of british anti-lewisite (bal). *Br. Med. Bull.* 5 (4–5), 313–318. <https://doi.org/10.1093/oxfordjournals.bmb.a073250>.
- Stone, H., See, D., Smiley, A., Ellingson, A., Schimmoeller, J., Oudejans, L., 2016. Surface decontamination for blister agents Lewisite, sulfur mustard and agent yellow, a Lewisite and sulfur mustard mixture. *J. Hazard. Mater.* 314, 59–66. <https://doi.org/10.1016/j.jhazmat.2016.04.020>.
- Dandekar, A.A., Vora, D., Yeh, J.S., Srivastava, R.K., Athar, M., Banga, A.K., 2023. Enhanced transdermal delivery of n-acetylcysteine and 4-phenylbutyric acid for potential use as antidotes to lewisite. *AAPS PharmSciTech* 24 (3). <https://doi.org/10.1208/s12249-023-02527-6>.
- Ghosh, M., Banga, A.K., 2025. Formulation and evaluation of a transdermal drug-in-adhesive patch for lamotrigine delivery in potential epilepsy treatment. *J. Drug Delivery Sci. Technol.*, 107067 <https://doi.org/10.1016/j.jddst.2025.107067>.
- Bhattaccharjee, S.A., Junaid, M.S.A., Ghosh, M., Srivastava, R.K., Athar, M., Banga, A.K., 2025. Topical foam for simultaneous treatment and decontamination of chemical warfare agents on dermal exposure. *AAPS PharmSci. Tech.*
- Kshirsagar, S.M., Viswaroopan, N., Ghosh, M., Junaid, M.S.A., Haque, S., Khan, J., Muzaffar, S., Srivastava, R.K., Athar, M., Banga, A.K., 2024. Development of 4-phenylbutyric acid microsponge gel formulations for the treatment of lewisite-mediated skin injury. *Drug Deliv. Transl. Res.* <https://doi.org/10.1007/s13346-024-01620-y>.
- Sintov, A.C., Shapiro, L., 2004. New microemulsion vehicle facilitates percutaneous penetration in vitro and cutaneous drug bioavailability in vivo. *J. Control. Release* 95 (2), 173–183. <https://doi.org/10.1016/j.jconrel.2003.11.004>.
- Li, C., Srivastava, R.K., Athar, M., 2016. Biological and environmental hazards associated with exposure to chemical warfare agents: arsenicals. *Ann. N. Y. Acad. Sci.* 1378 (1), 143–157. <https://doi.org/10.1111/nyas.13214>.
- Ghosh, M., Hazarika, P., Dhanya, S.J., Pooja, D., Kulhari, H., 2024. Exploration of sialic acid receptors as a potential target for cancer treatment: A comprehensive review. In: *International Journal of Biological Macromolecules*, vol. 257. Elsevier B.V. <https://doi.org/10.1016/j.jbiomac.2023.128415>.
- Vora, D., Dandekar, A.A., Srivastava, R.K., Athar, M., Banga, A.K., 2022. Development and evaluation of a topical foam formulation for decontamination of warfare agents. *Mol. Pharm.* 19 (12), 4644–4653. <https://doi.org/10.1021/acs.molpharmaceut.2c00636>.
- Kumar, M., Thakur, A., Mandal, U.K., Thakur, A., Bhatia, A., 2022. Foam-based drug delivery: a newer approach for pharmaceutical dosage form. *AAPS PharmSciTech* 23 (7). <https://doi.org/10.1208/s12249-022-02390-x>. Springer Science and Business Media Deutschland GmbH.
- Alkhailfah, M., Kalam, M.A., Raish, M., Ansari, M.A., Alsaleh, N.B., Almomani, A., Ali, R., Alshamsan, A., 2023. Topical sustained-release dexamethasone-loaded chitosan nanoparticles: assessment of drug delivery efficiency in a rabbit model of endotoxin-induced uveitis. *Pharmaceutics* 15 (9). <https://doi.org/10.3390/pharmaceutics15092273>.
- Michailidou, G., Christodoulou, E., Nanaki, S., Barmpalexis, P., Karavas, E., Vergkizi-Nikolakaki, S., Bikaris, D.N., 2019. Super-hydrophilic and high strength polymeric foam dressings of modified chitosan blends for topical wound delivery of chloramphenicol. *Carbohydr. Polym.* 208, 1–13. <https://doi.org/10.1016/j.carbpol.2018.12.050>.
- Al-Kassas, R., Wen, J., Cheng, A.E.M., Kim, A.M.J., Liu, S.S.M., Yu, J., 2016. Transdermal delivery of propranolol hydrochloride through chitosan nanoparticles dispersed in mucoadhesive gel. *Carbohydr. Polym.* 153, 176–186. <https://doi.org/10.1016/j.carbpol.2016.06.096>.
- Ma, J., Wang, Y., Lu, R., 2022. Mechanism and Application of Chitosan and Its Derivatives in Promoting Permeation in Transdermal Drug Delivery Systems: A Review. *Pharmaceutics* 15 (4), MDPI. <https://doi.org/10.3390/ph15040459>.
- Jafernik, K., Ładniak, A., Blicharska, E., Czarnek, K., Ekiert, H., Więcek, A.E., Szopa, A., 2023. Chitosan-based nanoparticles as effective drug delivery systems—a review. *Molecules* 28 (4), MDPI. <https://doi.org/10.3390/molecules28041963>.
- Abdel-Hafez, S.M., Hathout, R.M., Sammour, O.A., 2018. Tracking the transdermal penetration pathways of optimized curcumin-loaded chitosan nanoparticles via confocal laser scanning microscopy. *Int. J. Biol. Macromol.* 108, 753–764. <https://doi.org/10.1016/j.ijbiomac.2017.10.170>.
- Ta, Q., Ting, J., Harwood, S., Browning, N., Simm, A., Ross, K., Olier, I., Al-Kassas, R., 2021. Chitosan nanoparticles for enhancing drugs and cosmetic components penetration through the skin. *Eur. J. Pharm. Sci.* 160. <https://doi.org/10.1016/j.ejps.2021.105765>.
- Hasanovic, A., Zehl, M., Reznicek, G., Valenta, C., 2009. Chitosan-tripolyphosphate nanoparticles as a possible skin drug delivery system for aciclovir with enhanced stability. *J. Pharm. Pharmacol.* 61 (12), 1609–1616. <https://doi.org/10.1211/jpp.61.12.0004>.
- Radmard, A., Kumar Srivastava, R., Shrestha, N., Khan, J., Muzaffar, S., Athar, M., Banga, A.K., 2024. Enhancing topical delivery of ISRB: optimizing cream formulations with chemical enhancers and pH adjustment. *Int. J. Pharm.* 665. <https://doi.org/10.1016/j.ijpharm.2024.124661>.
- Srivastava, R.K., Mishra, B., Muzaffar, S., Gorbatyuk, M.S., Agarwal, A., Mukhtar, M.S., Athar, M., 2021. Dynamic regulation of the nexus between stress granules, roquin, and regnase-1 underlies the molecular pathogenesis of warfare vesicants. *Front. Immunol.* 12, 809365. <https://doi.org/10.3389/fimmu.2021.809365>.
- Srivastava, R.K., Wang, Y., Khan, J., Muzaffar, S., Lee, M.B., Weng, Z., Croutch, C., Agarwal, A., Deshane, J., Athar, M., 2022. Role of hair follicles in the pathogenesis of arsenical-induced cutaneous damage. *Ann. N. Y. Acad. Sci.* 1515 (1), 168–183. <https://doi.org/10.1111/nyas.14809>.
- Srivastava, R.K., Traylor, A.M., Li, C., Feng, W., Guo, L., Antony, V.B., Schoeb, T.R., Agarwal, A., Athar, M., 2018. Cutaneous exposure to lewisite causes acute kidney injury by invoking DNA damage and autophagic response. *Am. J. Physiol. Renal Physiol.* 314 (6), F1166–F1176. <https://doi.org/10.1152/ajprenal.00277.2017>.
- Srivastava, R.K., Muzaffar, S., Khan, J., Traylor, A.M., Zmijewski, J.W., Curtis, L.M., George, J.F., Ahmad, A., Antony, V.B., Agarwal, A., Athar, M., 2020. Protective role of HO-1 against acute kidney injury caused by cutaneous exposure to arsenicals. *Ann. N. Y. Acad. Sci.* 1480 (1), 155–169. <https://doi.org/10.1111/nyas.14475>.
- Decontamination of Chemical Wa.* n.d.
- Kshirsagar, S., Dandekar, A., Srivastava, R.K., Khan, J., Muzaffar, S., Athar, M., Banga, A.K., 2023. Microneedle-mediated transdermal delivery of N-acetyl cysteine as a potential antidote for lewisite injury. *Int. J. Pharm.* 647. <https://doi.org/10.1016/j.ijpharm.2023.123547>.
- Hussain, Z., Katas, H., Amin, M.C.I.M., Kumolosasi, E., Sahudin, S., 2014. Downregulation of immunological mediators in 2,4-dinitrofluorobenzene-induced atopic dermatitis-like skin lesions by hydrocortisone-loaded chitosan nanoparticles. *Int. J. Nanomed.* 9 (1), 5143–5156. <https://doi.org/10.2147/JN.S71543>.
- Nair, R.S., Morris, A., Billa, N., Leong, C.O., 2019. An evaluation of curcumin-encapsulated chitosan nanoparticles for transdermal delivery. *AAPS PharmSciTech* 20 (2). <https://doi.org/10.1208/s12249-018-1279-6>.
- Herdiana, Y., Febrina, E., Nurhasanah, S., Gozali, D., Elamin, K.M., Wathoni, N., 2024. Drug Loading in Chitosan-Based Nanoparticles. *Pharmaceutics* 16 (8), 1043. <https://doi.org/10.3390/pharmaceutics16081043>.
- Matos, B.N., Reis, T.A., Gratiere, T., Gelfuso, G.M., 2015. Chitosan nanoparticles for targeting and sustaining minoxidil sulphate delivery to hair follicles. *Int. J. Biol. Macromol.* 75, 225–229. <https://doi.org/10.1016/j.ijbiomac.2015.01.036>.
- Phatale, V., Vaiphei, K.K., Jha, S., Patil, D., Agrawal, M., Alexander, A., 2022. Overcoming skin barriers through advanced transdermal drug delivery approaches. *J. Controlled Release* 351, 361–380. <https://doi.org/10.1016/j.jconrel.2022.09.025>.
- Szymańska, E., Winnicka, K., 2015. Stability of chitosan—a challenge for pharmaceutical and biomedical applications. *Mar. Drugs* 13 (4), 1819–1846. <https://doi.org/10.3390/md13041819>.
- Kumar Jangid, A., Solanki, R., Ghosh, M., Jadav, M., Patel, S., Pooja, D., Kulhari, H., 2023. Phenylboronic acid conjugated PAMAM G4 dendrimers augmented usnic acid delivery to gastric cancer cells. *Eur. Polym. J.* 192. <https://doi.org/10.1016/j.eurpolymj.2023.112073>.
- Ahmed, M.E., Mohamed, M.I., Ahmed, H.Y., Elaasser, M.M., Kandile, N.G., 2024. Fabrication and characterization of unique sustain modified chitosan nanoparticles for biomedical applications. *Sci. Rep.* 14 (1), 13869. <https://doi.org/10.1038/s41598-024-64017-4>.
- Kumar, K., Rawat, S.G., Manjiti, M.M., Priya, Kumar A., Chawla, R., 2023. Dual targeting pH responsive chitosan nanoparticles for enhanced active cellular internalization of gemcitabine in non-small cell lung cancer. *Int. J. Biol. Macromol.* 249. <https://doi.org/10.1016/j.ijbiomac.2023.126057>.
- Şenyiğit, T., Sonvico, F., Barbieri, S., Özer, Ö., Santi, P., Colombo, P., 2010. Lecithin/chitosan nanoparticles of clobetasol-17-propionate capable of accumulation in pig skin. *J. Control. Release* 142 (3), 368–373. <https://doi.org/10.1016/j.jconrel.2009.11.013>.
- Kshirsagar, S.M., Shrestha, N., Kipping, T., Banga, A.K., 2024. Formulation development of tazarotene-loaded PLGA nanoparticles for follicular delivery in the treatment of inflammatory skin diseases. *Eur. J. Pharm. Biopharm.* 200, 114346. <https://doi.org/10.1016/j.ejpb.2024.114346>.